Chapter 1 Introduction

1.1Motivation

Recently, large demand for wireless communication devices is increasing and the Radio Frequency Integrated Circuit (RFIC) devices such as LNA [1], VCO [2], band pass filters [3] are widely incorporated with micro-electro-mechanical systems (MEMS) passives based on CMOS process. Spiral inductors are usually the most critical passives in the RFICs but they would occupy most of the circuit chip area which is the key factor to determine the cost of the communication devices. Therefore, how to reduce the size of spiral inductors without having any inductance degradation in the chip has become one of research topics in RFICs. Previous researches have shown that spiral inductors with ferromagnetic cores can be a promising candidate to replace the existing on-chip spiral inductors.

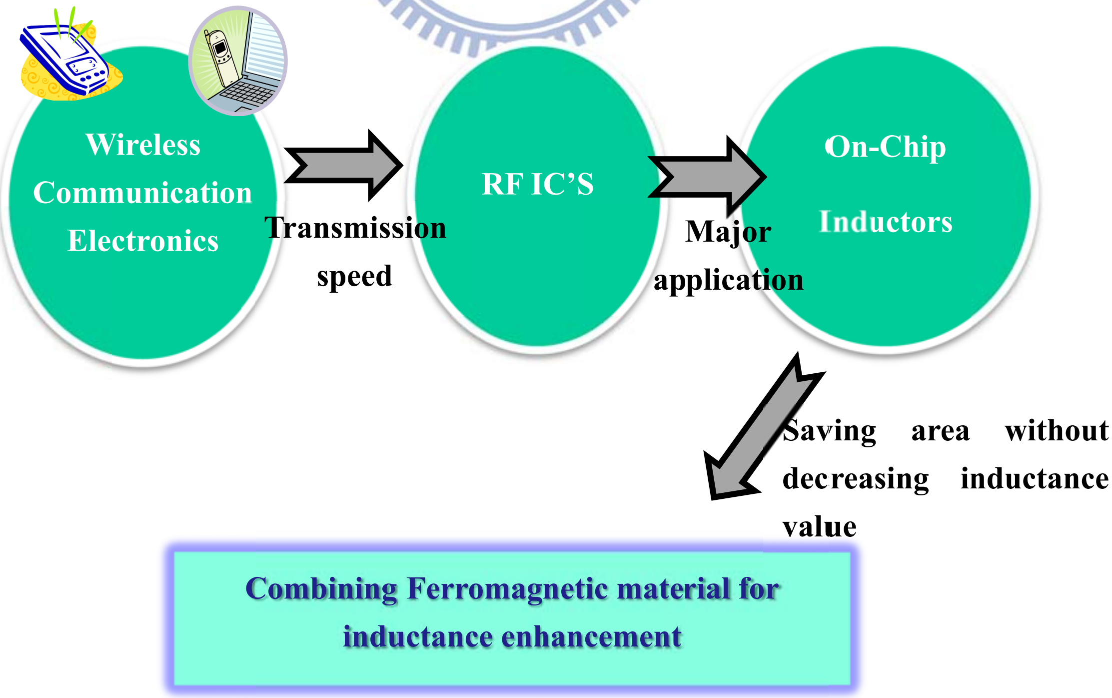

Fig. 1-1-1: The development of ferromagnetic inductor.

However, this idea is usually accompanied with two major challenges; eddy current loss (ECL) and ferromagnetic resonance (FMR) which are two main loss mechanisms in ferromagnetic material

Due to the generation of time varying magnetic field in the on-chip inductors, eddy current will be induced within the substrate and the ferromagnetic material. In order to reduce ECL, patterning the ferromagnetic material into small segments has been a considerable choice [4]. Our previous work has proposed an approach for the synthesis of ferromagnetic and AAO [5], therefore, the eddy current is restricted in a small area which is in an order of nm^2. The average power loss of a cylindrical magnetic layer with radius *a* is represented by $P_{r=a}$, and is illustrated in Fig. 1-1-2.

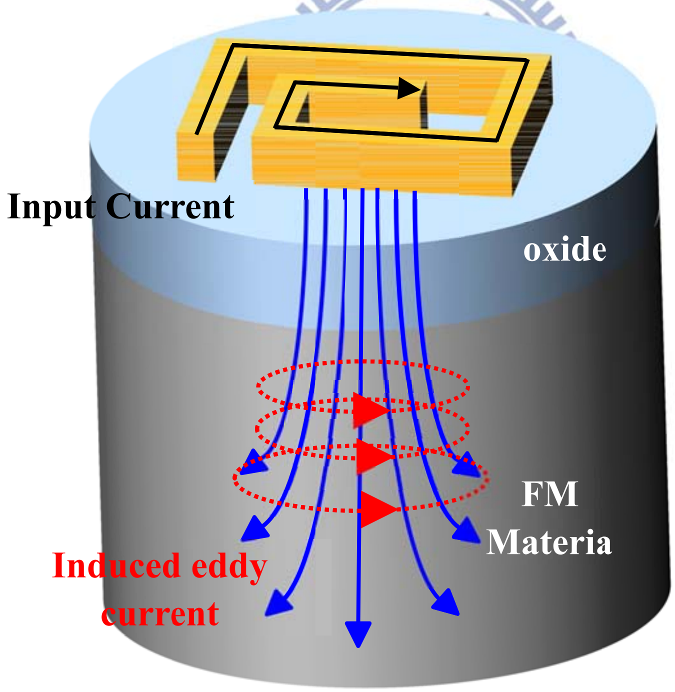

Fig. 1-1-2: The first case of the eddy current loss, while the underlying ferromagnetic material is in the shape of cylindrical with r=a

If the time varying magnetic field generated by inductor itself is in the form:

$$B(t) = B_0 \sin \omega t \tag{1}$$

Then the electromotive force is generated due to the variation of magnetic flux density and is in the form:

$$V = \frac{d\phi}{dt} = \pi r^2 \omega B_0 \cos \omega t \qquad (2)$$

So, the total power loss $P_{r=a}$ of this case can be derived by the following:

$$P_{r=a} = \int dP = \int d(\frac{V^2}{R}) = \int_{r=o}^{r=a} \frac{(\pi r^2 \omega B_0 \cos \omega t)^2}{2\pi r / \sigma h \cdot dr}$$

$$= \frac{1}{8} \sigma \pi h a^4 \omega^2 B_0{}^2 \cos^2 \omega t \qquad (3)$$

Where r is radius of cylindrical FM material, h is cylinder height and σ is the conductivity of FM material.

Let's consider the eddy current loss of another case. If we pattern the FM into N well-isolated cylindrical with r=b as illustrated in Fig. 1-1-3.

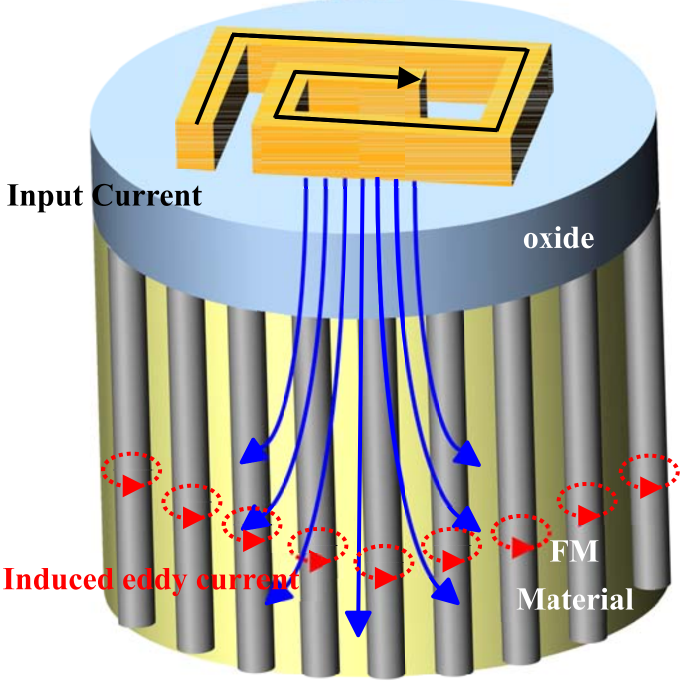

Fig. 1-1-3: The second case of the eddy current loss, while the underlying ferromagnetic material is in the shape of N isolated cylindrical with r=b

The power loss $P_{r=b}$ in this case can be derived similarly as following:

$$P_{r=b} = \frac{N}{8}\sigma\pi h b^{4}\omega^{2}B_{0}^{2}\cos^{2}\omega t \qquad (4)$$

The relationship between these two cases is described by the following equation:

$$P_{r=b} = N\frac{b^{4}}{a^{4}}P_{r=a} \cong \frac{b^{2}}{a^{2}}P_{r=a} \qquad (5)$$

It can be simplified if we make an assumption that the total conducting areas are the same for both two cases, i.e.$N\pi b^{2}=\pi a^{2}$. It can be observed that the ECL is suppressed due to b<<a.

FMR is another limiting factor of ferromagnetic material application in RF range and it can be calculated by the following:

$$f_{FMR} \cong \frac{\gamma}{2\pi}\sqrt{H_{k}(H_{k}+4\pi M_{s})} \qquad (6)$$

Where γ is gyromagnetic ratio, H_k is the effective anisotropy magnetic field, and M_S is the saturation magnetization [6]. From this equation we can improve the FMR by choosing the material with high M_S and large shape anisotropy to obtain high H_k. The porous of AAO template is about 65nm in diameter and is 1000nm in length, so a high aspect ratio can be easily achieved without being limited by the resolution of lithography process, with this advantage, we can satisfy the requirement of large shape anisotropy.

1.2Historical Review

Besides, we also need to choose a material with high saturation magnetization. In the original scheme, we utilized Ni to fabricated the nanorod array by electroless deposition[6]. Nevertheless, large P content(~15%) inside the alloy will enlarge the inter-atomic distance and cause smaller saturation magnetization. Unfortunately, the inductance enhancement is not apparent(about 3%) as shown in Fig. 1-2-1. So NiFe permalloy here is chosen to substitute for electrolessplating Ni due to its high relative permeability(μ_r)

Previously, we demonstrated a spiral inductor using NiFe-AAO magnetic nancomposite core electroplated on a Ti seed-layer will end up with a large capacitance between inductor coil and the seed-layer[5]. Although the inductance can be successfully improved, smaller *Q* factor and resonance frequency are not expected. In order to resolve the issue, we utilized thermal treatment to anneal the nanocomposite core at 450^{o}C in a vacuum ambient in order to transform the conductive Ti layer into a less conductive TiO_x amorphous layer. Experimental results have shown that the *Q* factor can truly be improved, but the resonance frequency still remains the same as shown in Fig 1-2-2. It could be resulted by the annealing period which is not long enough to consume the whole Ti layer.

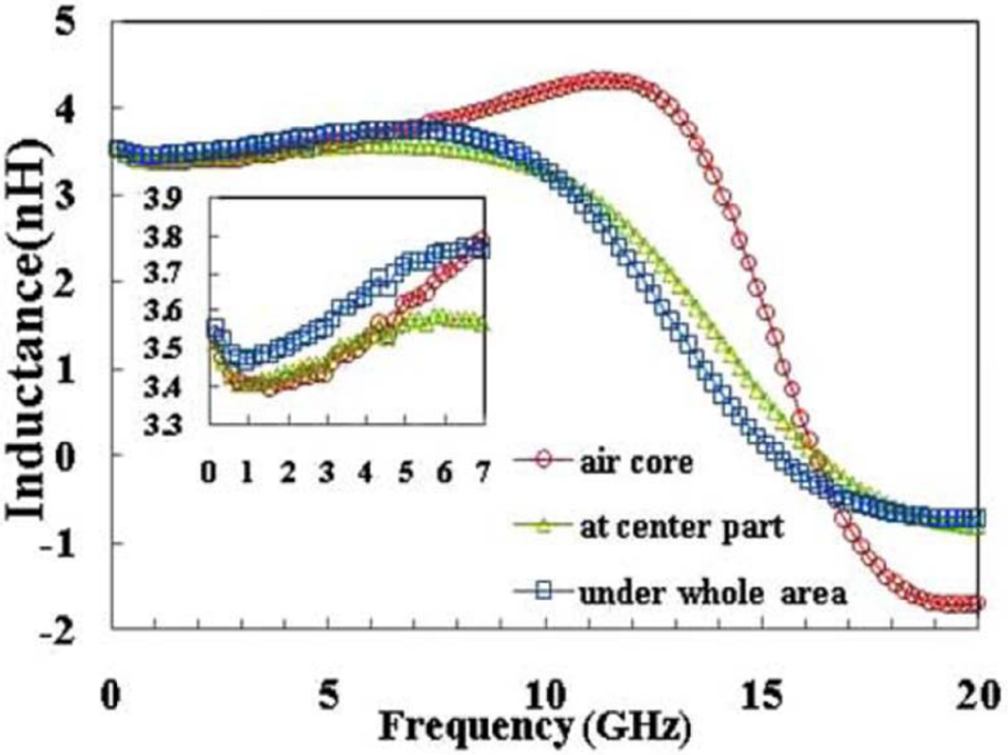

(a)

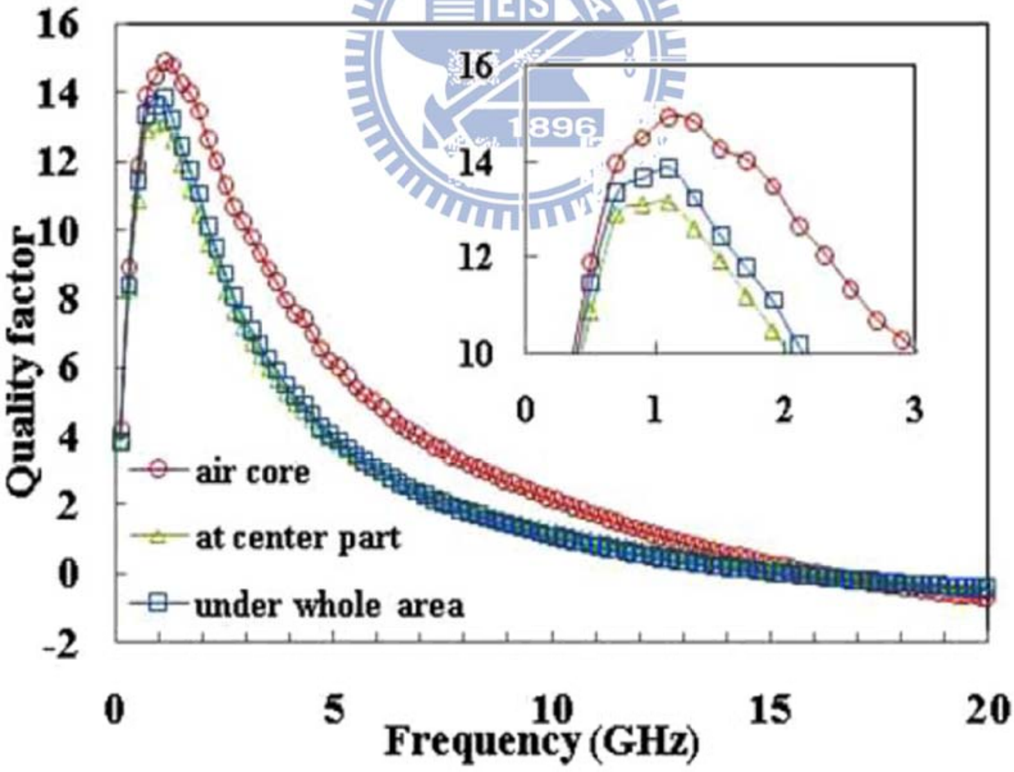

(b)

Fig. 1-2-1: The equivalent series inductance(a) and Quality factor(b) of Ni-AAO inductor which is designed with n=3.5, din=100um.

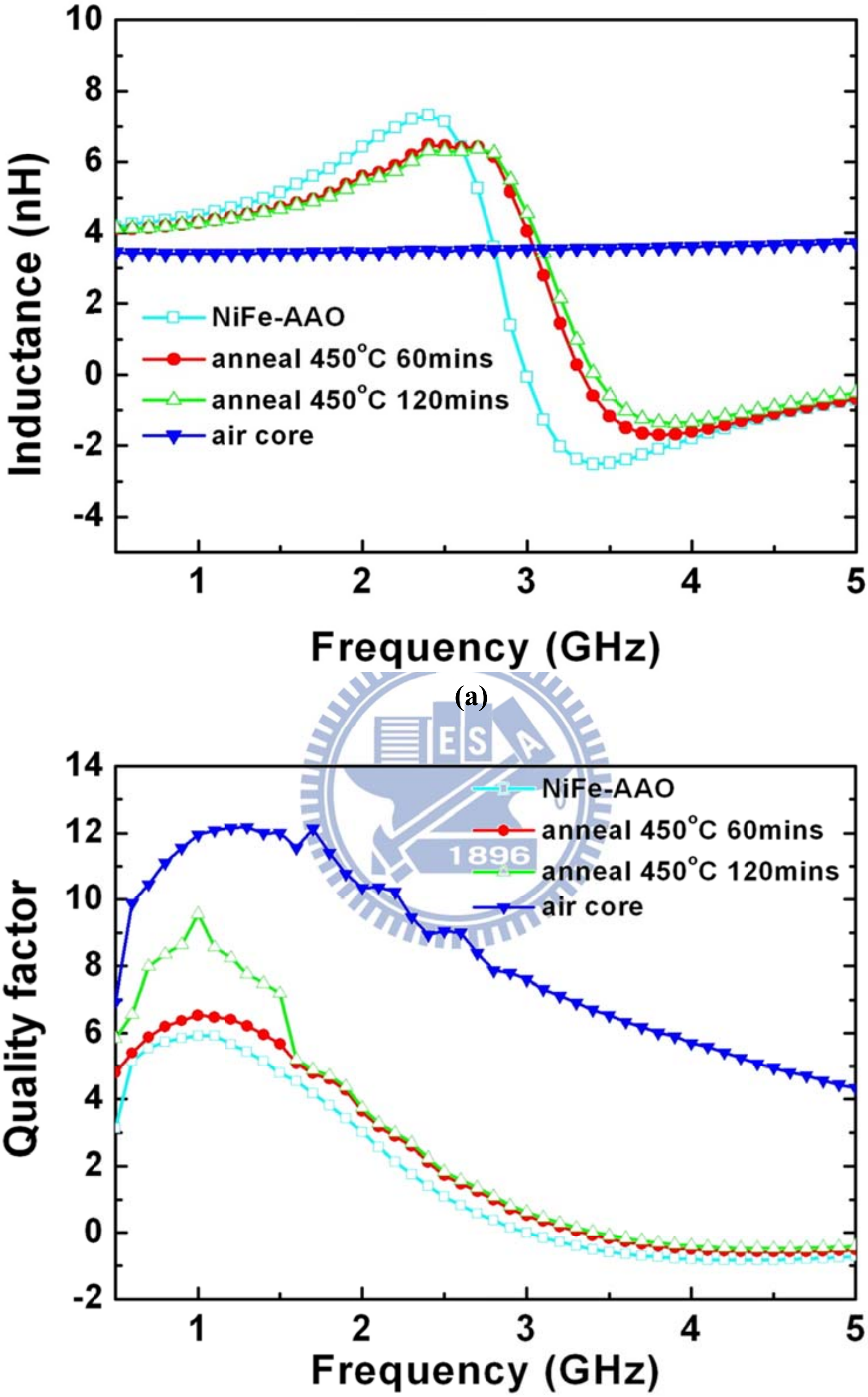

(a)

(b)

Fig. 1-2-2: The equivalent series inductance(a) and Quality factor(b) of NiFe-AAO inductor which is designed with n=3.5, din=100um.

In this work, we' will focus on a micromachining process designed to remove the Ti seed-layer instead of the thermal anneal. With one extra photolithography process step and one dry etching technique using XeF_2 to remove the Ti layer and underlying silicon substrate, a micromachined spiral inductor utilized NiFe-AAO nanocomposite core with better performance can be achieved at room temperature. The schematic 3-D cross section view of the MEMS inductor with NiFe-AAO nanocomposite cores is shown in Fig. 1-2-3.

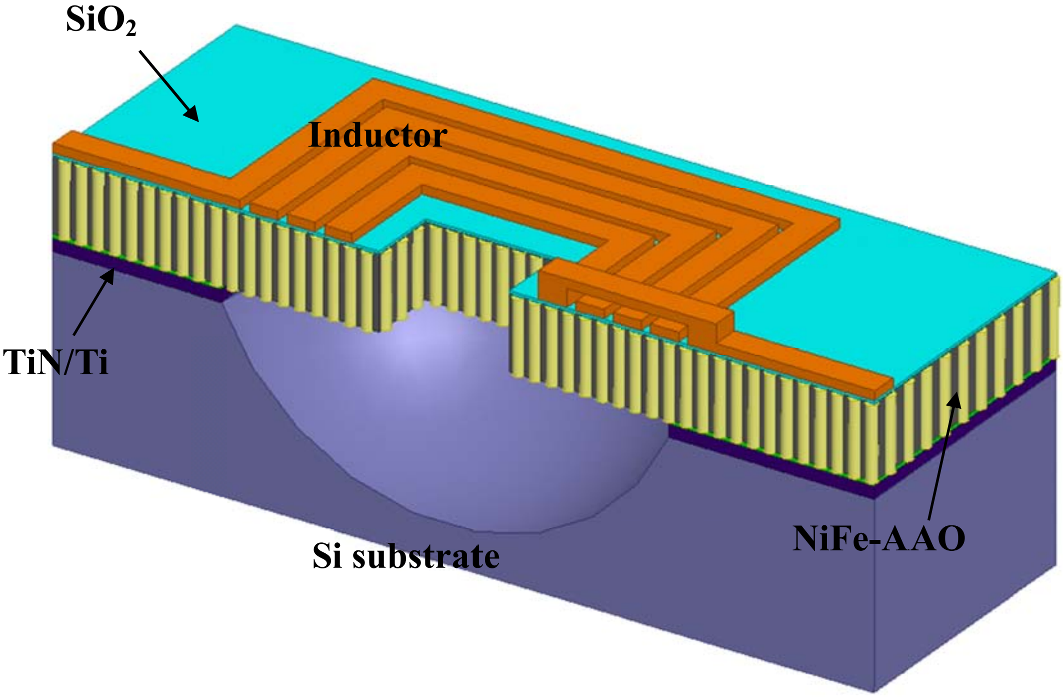

Fig. 1-2-3: The geometry of the MEMS structure inductor with NiFe-AAO nanocomposite core

Chapter 2 The Synthesis of the NiFe-AAO Nanocomposite and The Fabrication of Micromachined Spiral Inductors

2.1 Design of the Spiral Inductor

In this work, the inductors are designed with 3.5 turn spirals which are in the shape of rectangular. The geometry structure of the inductor is shown in Fig.2-1(a). The inter diameter(D_{in}) is 100µm and the metal coil is 15µm in width, 5µm in spacing distance(S) and 5µm in thickness. The material of inductor is chosen to be copper due to its characterization of high conductivity, meanwhile, the metal loss of inductor itself can be degraded when operates in higher frequency. Fig.2-1 (a) and (b) shows the geometry morphology of the rectangular spiral inductor. And we choose silicon dioxide as the electrical insulating layer which is 750nm in thickness and is placed between the silicon substrate the inductor. This structure is the typical inductor which is called "Air-core inductor", the following we are going to take it as reference to discuss how ferromagnetic material works on improving performance.

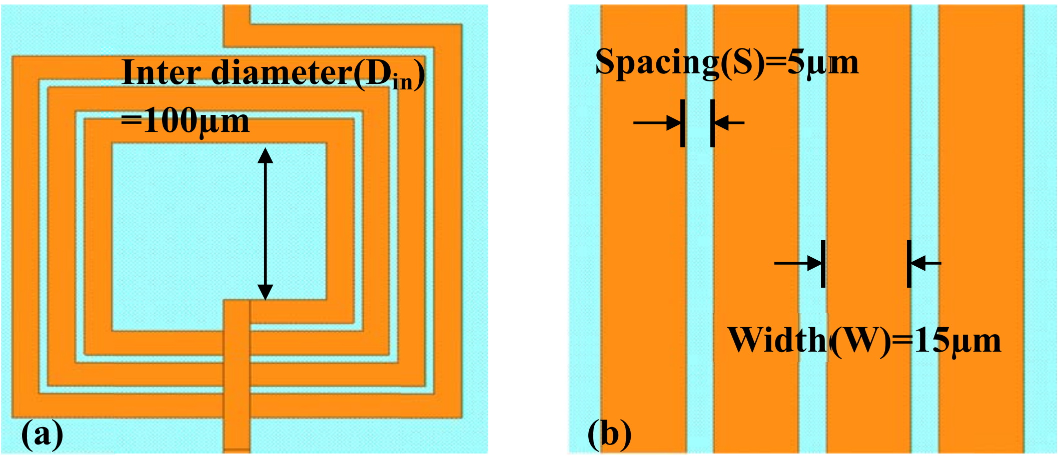

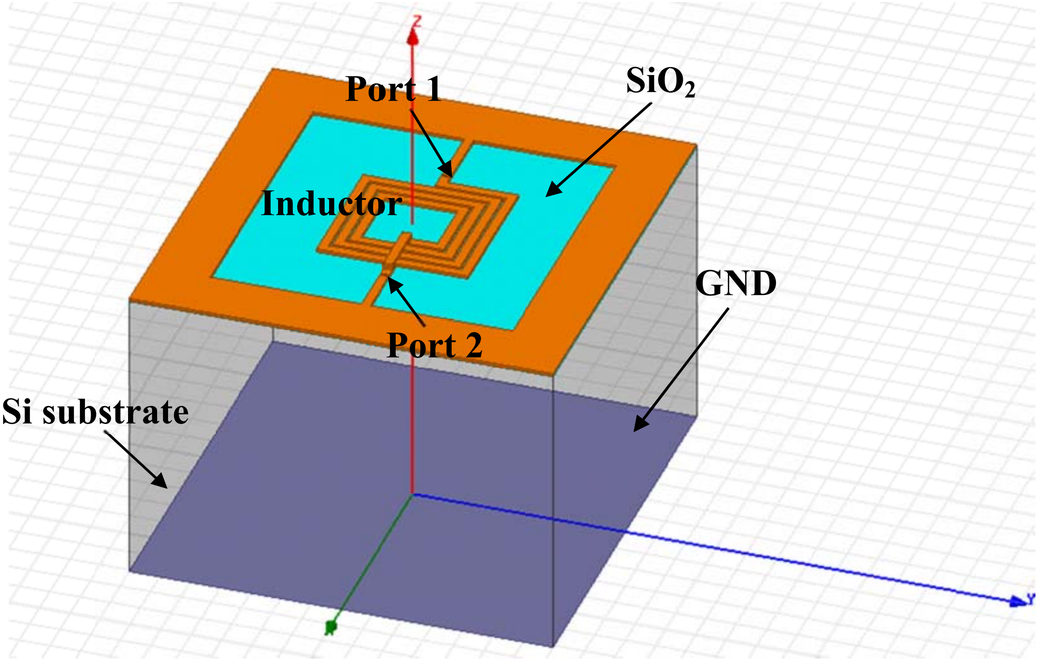

(c)

Fig.2-1-1. The spiral inductor design is shown in (a) and (b), and the total simulated condition of a air-core inductor is shown in (c)

A simulation software ANSOFT HFSS 13.0 is equipped for the high frequency range analysis. The total structure morphology is shown in Fig.2-1-1 (c). The simulation process is taken from 100MHz to 20GHz, the simulated results of inductance value and Quality factor is shown in Fig.2-1-2 (a) and (b). From the graph, the case of air-core spiral inductor is designed with the inductance value of about 3.3nH and the maximum value of Quality factor is about 12.5. The self-resonance of an inductor occurs due to the parasitic LC tank of itself, at Fig.2-2 (b), the self-resonance frequency happens at the point which the Quality factor is zero[7] and it is about 15GHz read from the graph. Besides, the simulated magnetic field distribution is shown in Fig.2-2 (c), it indicates that the magnetic field under the spiral coil is stronger than it is at the center of the inductor.

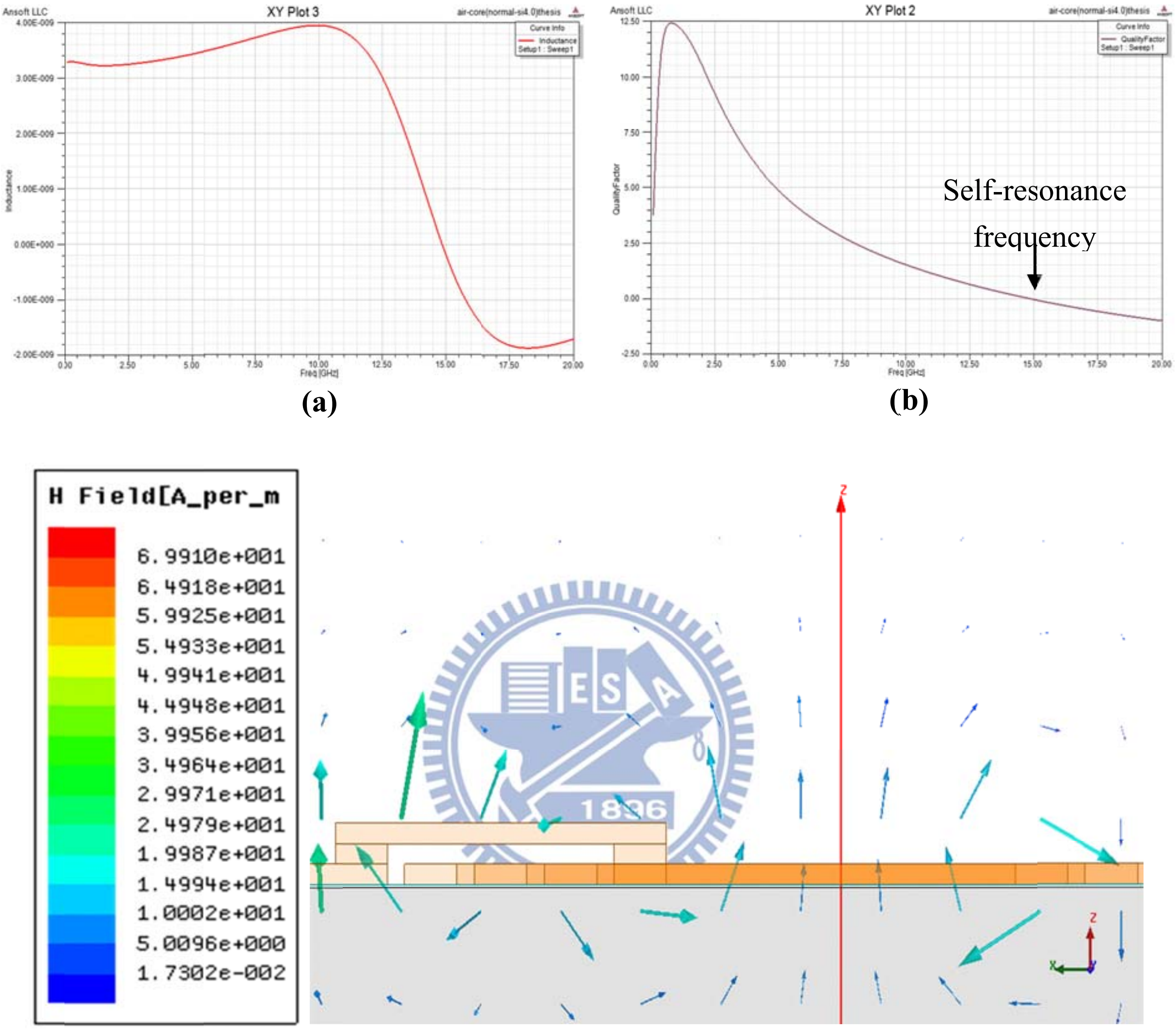

(a) **(b)**

(c)

Fig.2-1-2. Both simulated results including inductance value and Quality factor are shown in (a) and (b). The simulated magnetic field distribution is plotted in (c).

2.2 The Synthesis of NiFe-AAO Nanocomposite

The Porous anodic alumina oxide (AAO) template with self-organized hexagonal of uniform parallel nanopores has been widely utilized for the synthesis of one-dimensional nanostructures since 80's. Each cell contains cylindrical central pore normal to the substrate. Due to it's characteristic of deep pore, it is suitable for manufacturing the ferromagnetic nanorods within it. The magnetic nanorods of high aspect ratio provide large shape anisotropy so that the drawback of FMR can be diminished as we've mentioned before. The AAO template can be prepared by anodic oxidation of aluminum in various acid solutions and various anodizing conditions, such as temperature, applied voltage, widening time and current are used to control the pore diameter and length [8, 9]. In this work, the one step anodization method[10] is sufficient to fabricate the AAO template on silicon substrate in 0.3 M oxalic acid solution at 2℃ with a constant voltage 40V. During the period of anodic reaction, Pt film is chooed as the cathode, the total experiment setup is depicted in Fig.2-2-1.

The basic concept of the formation of the porous alumina oxide is illustrated in Fig.2-2-2(a)[11]. At the Al/Electrolyte interface, the aluminum ion is dissociated from the aluminum atom.

$$Al_{(s)} \rightarrow Al^{3+} + 3e^{-} \qquad \textbf{(7)}$$

Then the aluminum ion reacts with the hydroxide and transferred into alumina, so a thin aluminum oxide layer s formed between metal and electrolyte.

$$2Al^{3+} + 3OH^{-} \rightarrow Al_2O_3 + 3H^{+} \qquad \textbf{(8)}$$

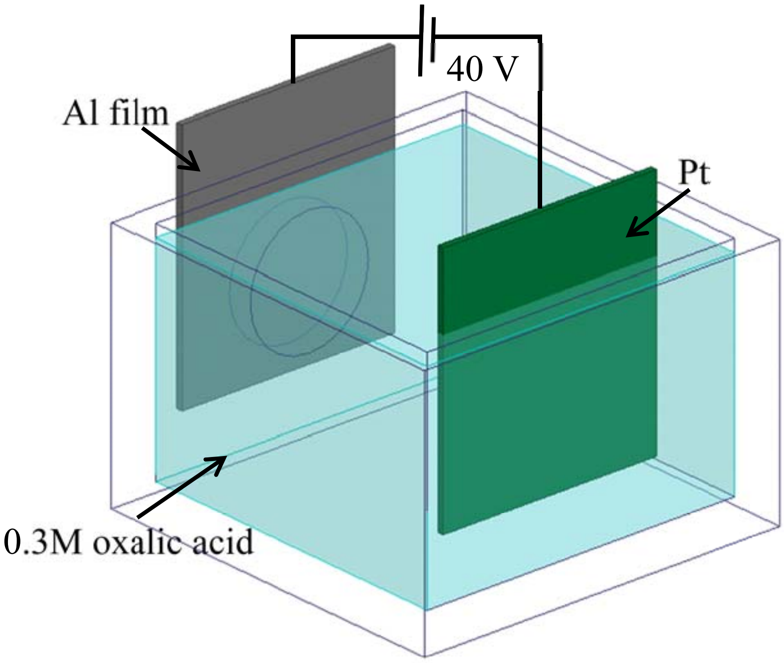

Fig.2-2-1. The anodization experiment setup diagram.

At the same time, the hydroxide ion is also penetrated through the oxide layer due to the attractive force of the positive anodic bias voltage, the penetrated hydroxide ion continue reacts with alumina ion and Al/Al_2O_3 interface starts to shift inward. Hydrogen ion generated in (8) and in the electrolyte will dissolve the aluminum oxide and turn it back to aluminum ion.

$$Al_2O_3 + 6H^+ \rightarrow 2Al^{3+} + 3H_2O \quad \textbf{(9)}$$

This is going to form the initial pore. Since local electric field intensity is the strongest at the bottom of the pore, the reaction of dissolving aluminum oxide is mainly focus on the pore bottom. The pore goes deeper as the reaction keeps going on and the rest aluminum continue to react with hydroxide to generate more hydrogen ion. The whole anodic reaction is completed when the residual aluminum is totally consumed.

The current during the reaction is related to different pore status which is presented in Fig.2-2-2(b). At point A, the current is still decreasing which means the reaction isn’t completed. Still needs more time to consume the residual aluminum. At point B which is located at the local maximum, reaction is almost done and the pore is directly opened to silicon substrate. At point C, the anodization is over react, all aluminum is totally transferred into aluminum oxide which causes the volume expansion of pore bottom. In this work, I stop the anodic reaction at point B, the SEM pictures of as-fabricated AAO template are presented in Fig.2-2-3 (a) and (b).

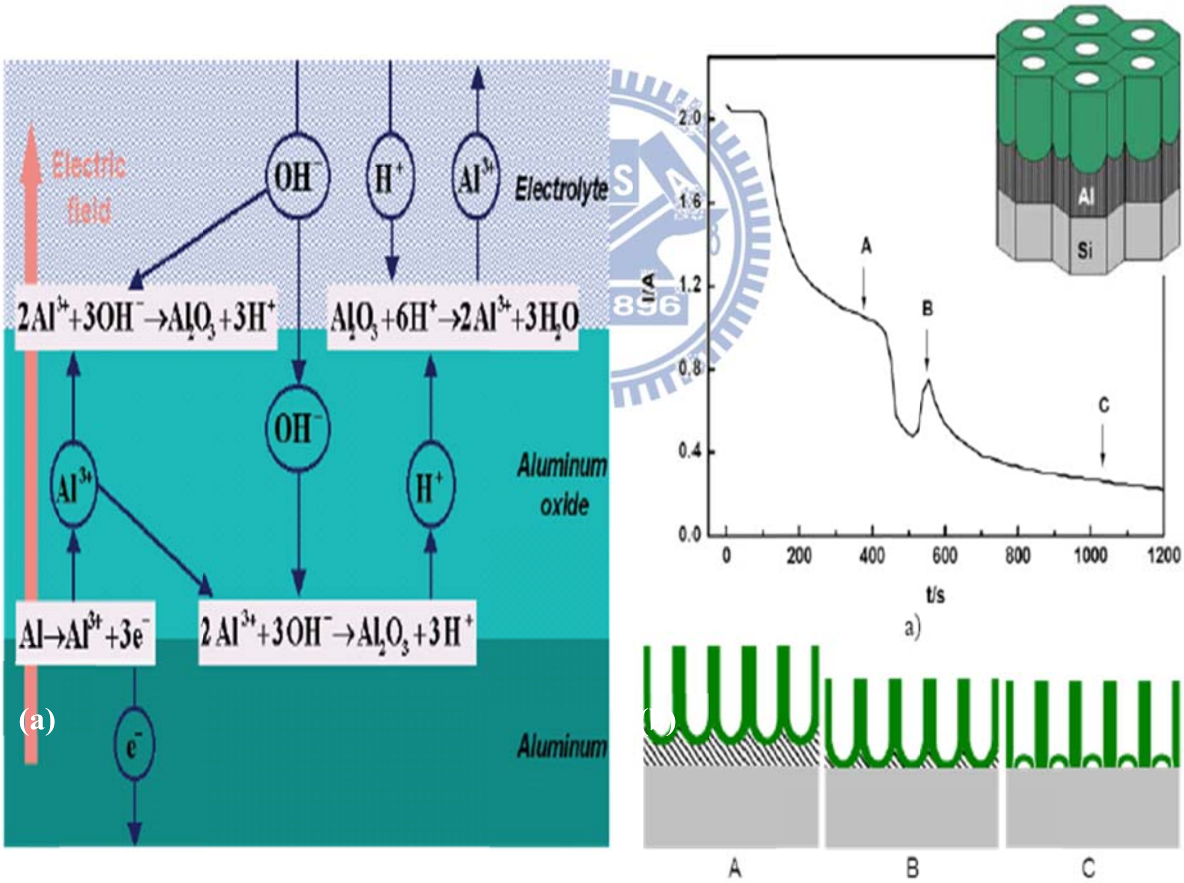

(a) **(b)**

Fig.2-2-2. The schematic diagram of the chemical reactions during the anodization is shown in (a), and the pore status with respect current is depicted in (b)

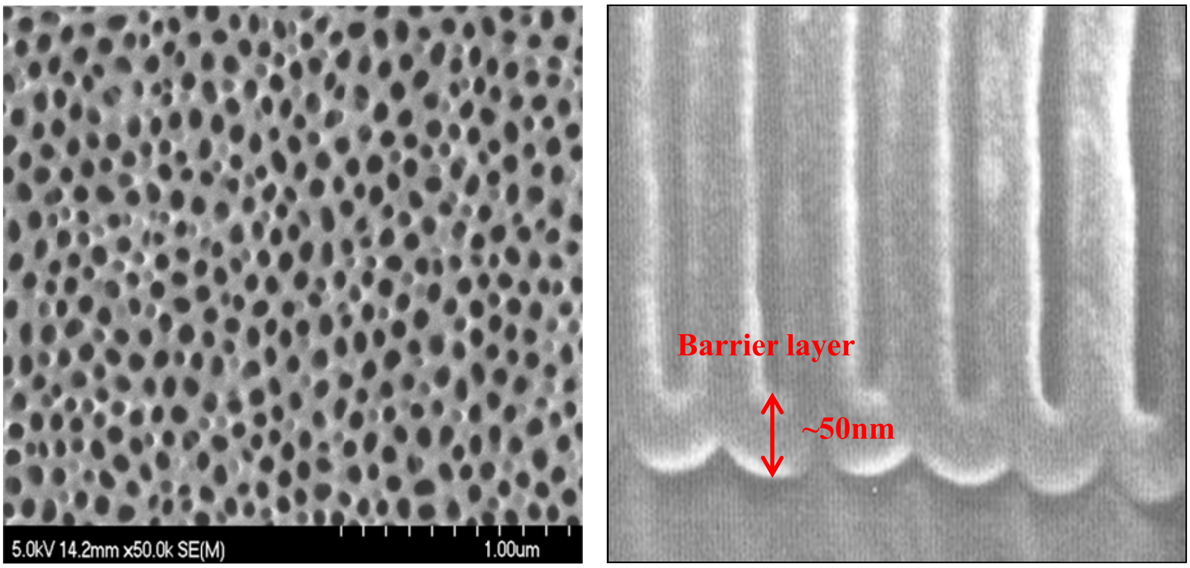

Fig.2-2-3 SEM pictures of the top view and the cross section view of the as-fabricated AAO template, and in (b), there is a barrier layer formed after the anodic reaction which is about 50nm in thickness

In Fig.2-2-3 (b) we can see there is a barrier layer which is also consisted with aluminum oxide formed at the bottom of the pore and it is about 50nm in thickness. This barrier inhibit the pore to directly open to the seed-layer underneath it, in the same time, this barrier layer also prohibit electroplating NiFe into these pores successfully. So the following, we need to take some extra treatment to remove the barrier.

The process flow of synthesis of NiFe-AAO nanocomposite is presented in Fig. 2-2-4. During the anodic reaction, we've found that the Ti seed-layer would easily be oxidized. This fact will end up in electroplating NiFe nanorods unsuccessfully. In this work we add an extra TiN layer on top of Ti as passivation to prevent being oxidized. Thus, a Ti(190nm)/TiN(15nm) bilayer is deposited on a 4" silicon wafer by sputter at first. Then a layer of Al(1000nm) is deposited by E-gun as shown in Fig.2-2-4 (a). The first step of anodic reaction is taking place in a 0.3M oxalic acid($H_2C_2O_4$) solution at 2^{o}C with a anode bias of 40V as shown in Fig.2-2-4 (b). The low temperature anodization process can reduce excessive current flow and heat evolution to make the AAO with the characteristic of small-pore films[12]. The first step anodization takes about 26 min and then reduces the bias voltage from 40V to 0V by the rate of 1V/min for creating some penetrating paths on the alumina oxide barrier layer as shown in Fig.2-2-4 (c)[13]. For further eliminating the barrier layer, adding a reverse-bias voltage (~-2.5V) to substrate in a 0.5M KCl solution at 2^oC for 15min as shown in Fig.2-2-4 (d)[12,14]. At this moment, KCl solution can go through the penetration paths so that it can react effectively. Finally, immersing the AAO substrate in a 5% H_3PO_4 solution at 30°C for 25 min as shown in Gig.2-2-4 (e) and uniformly distributed nanopores with about 60nm in diameter can be obtained. And each pore is directly opened to TiN layer to ensure NiFe nanorods can be filled with every pore successfully.

Embedding NiFe into AAO template is relied on electroplating process. In this work, fixed direct current(DC) method is employed with the current density of $5mA/cm^2$. The content of NiFe solution bath is presented in Table. 2-1. The temperature of the electrolyte is maintained at 30°C during the electroplating process and the schematic of depositing NiFe into AAO template is shown in Fig. 2-2-4 (f).

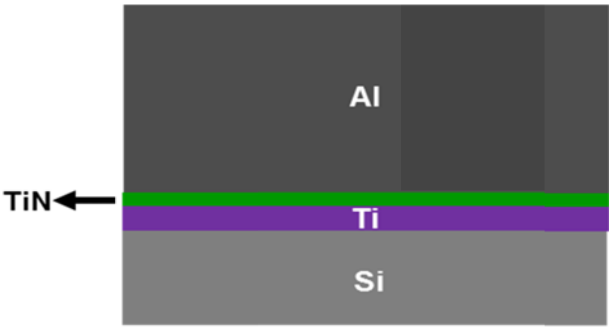

(a)

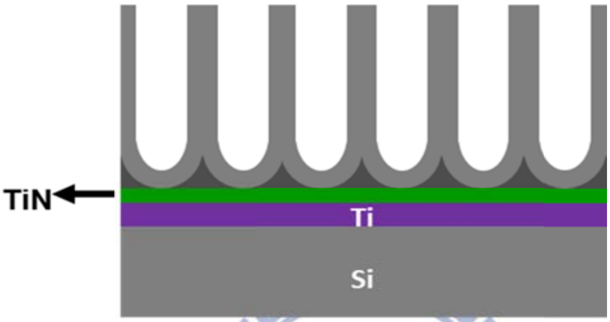

(b)

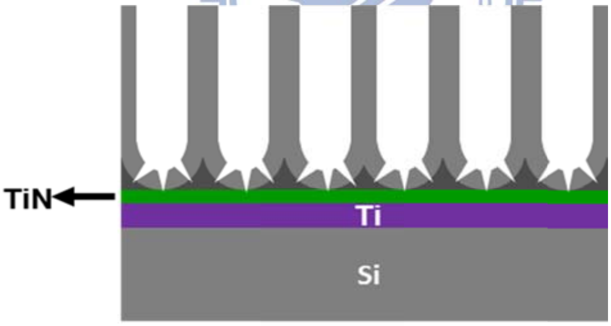

(c)

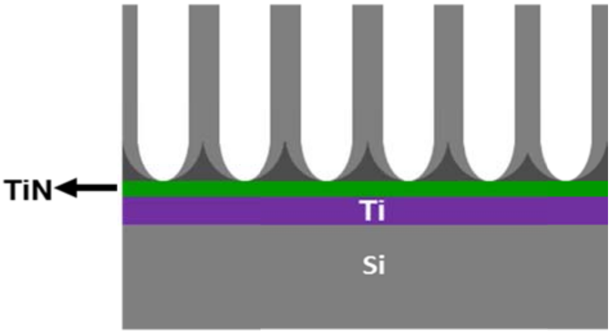

(d)

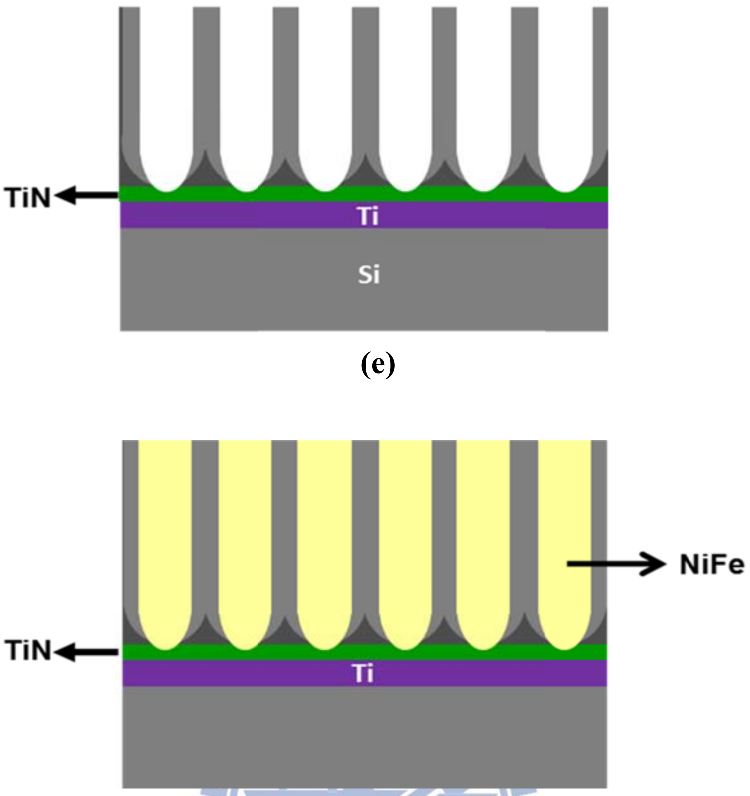

(e)

(f)

Fig. 2-2-4. The process flow of synthesizing NiFe-AAO starts with depositing Ti/TiN/Al on silicon substrate respectively as shown in (a), so that it is prepared for the initial anodization reaction just as (b). For thinning the barrier layer, dropping the anodic voltage from 40V to 0V to create some penetration paths on the barrier layer like (c) shows. Next step, another electro-chemical etching process is utilized to remove the barrier layer by switching the electrodes in the 0.5M KCl solution. Then immersing the sample in 5% H_3PO_4 for widening the pore diameter as shown in (e) so NiFe can be successfully deposited into the AAO template like (f) shows.

Content	**Concentration**
Nickel sulfate (g/l)	200
Iron sulfate (g/l)	8
Nickel chloride (g/l)	5
Boric acid (g/l)	25
Saccharin (g/l)	2
Sodium lauryl sulfate (g/l)	0.1
Deposition temperature (℃)	28
pH value	3

Table.2-1 The content of the NiFe electrolyte.

The SEM pictures in Fig. 2-2-5 presents the top view and the cross-section view of the NiFe-AAO nanocomposite. From (a), the pore diameter(r) is about 65nm and the inter-pore distance(d) is about 100nm. From (b), the length of the NiFe nanorod is about 950nm. These parameters are going to be useful when discussing the characterization of nanocomposite in the next chapter.

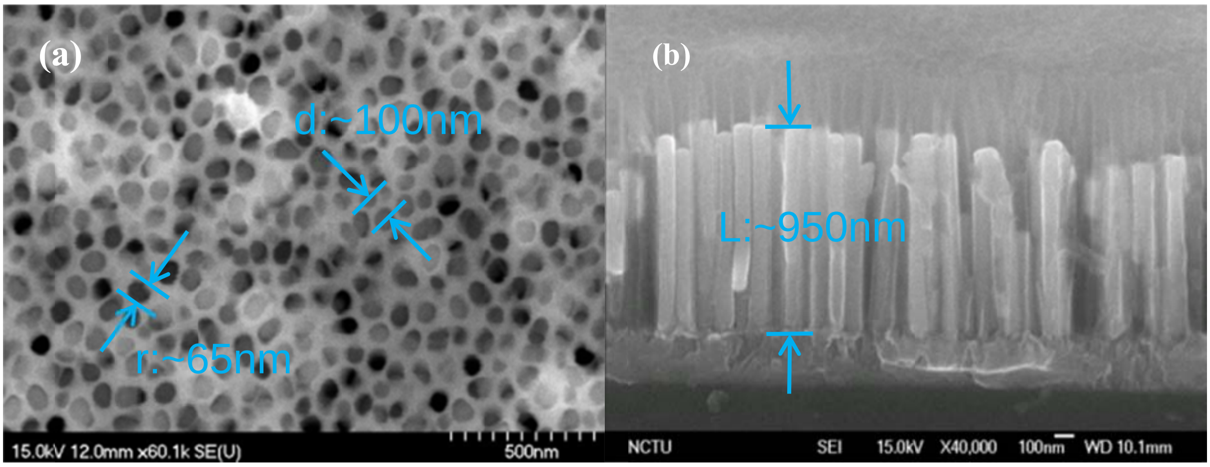

Fig. 2-2-5: The SEM micrograph promote the (a) top view and (b) cross section view of NiFe nanorods.

2.3 MEMS Strucrure Inductor Imcoporated with NiFe-AAO Nanocomposite

Once the NiFe-AAO nanocomposite is prepared, then we can start to combine it with spiral inductors. The spiral inductors of 3.5 turns are made of 5-um-thick electroplated Cu and designed with 100 um in inter diameter, 15 um in line width, and 5 um in line space have been utilized for the investigation of inductance enhancement with NiFe nanorods as the magnetic core. Fig. 2-3-1 is going to demonstrate the fabrication process of the on–chip spiral inductors with NiFe-AAO nanocomposite and finally obtain a MEMS structure inductor for improving the performance. It begins with NiFe-AAO template is fabricated using the aforementioned as mentioned before which is shown in Fig. 2-3-1 (a). A layer of 0.2-um-thick-SiO_2 is deposited on the top of the composite film by PECVD as an electrical insulation layer, and then followed by sputtering Cr/Cu (500Å/1000Å) adhesion/seed layer which is shown in Fig. 2-3-1(b). So far we've done are the prior preparation for the fabrication of spiral inductor. Moving to the inductor fabrication, first, a 1st 6-um thick AZ 4620 photo-resist is coated and patterned to define the region for inductor coil of spiral inductor, and a 5-um-thick Cu coil is electroplated as shown in Fig. 2-3-1(c). Then the 2nd 10-um thick AZ 4620 is spin coated, patterned and defined the region of inductor via, 5-um-thick Cu via is formed by electroplating as shown in Fig. 2-3-1(d). Sputtered with 150nm Cu seed layer as shown in Fig. 2-3-1(e). Fig. 2-3-1(f) shows the 3rd 6-um AZ 4620 is coated on top of Cu seed-layer and patterned to define the region of air bridge, and plated with 5um-thick Cu to define air bridge. Removing the sacrificial photo-resist and lifting off the underneath copper seed layer and chemically etch away the first seed/adhesion layer using Cu etchant (100:5:5 wt. water: acetic acid: hydrogen peroxide)/Cr etchant (diluted HCl)the Cr/Cu seed-layer, we can get the as-fabricated NiFe-AAO inductor as shown in Fig. 2-3-1(g).

(a)NiFe-AAO template is prepared

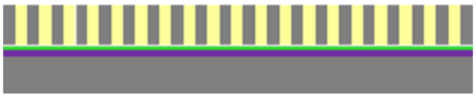

(b)deposite SiO2 insulating layer and Cr/Cu seed layer

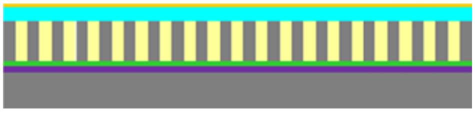

(c)1st mask defines inductor coil pattern

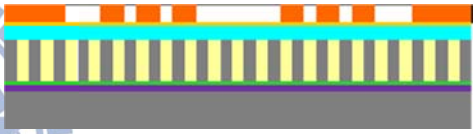

(d)Coating 2nd PR layer to define the via hole

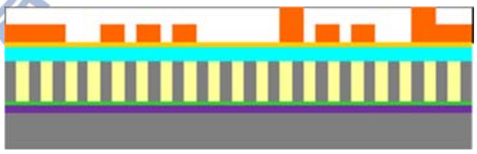

(e)Covered Cu seed-layer by sputter

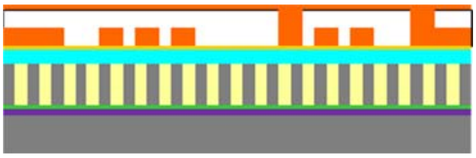

(f)Coating 3rd PR layer to define the air bridge

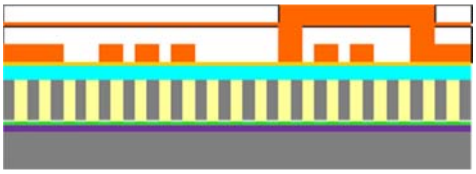

(g)After PR and seed layer removal, NiFe-AAO inductor is obtained

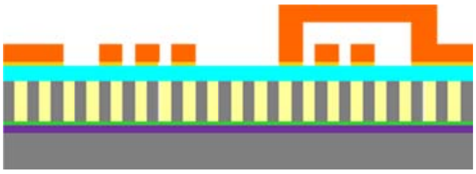

Fig. 2-3-1. The process flow of micromachined inductor incorporated with NiFe-AAO nanocomposite, step (a) to (g) demonstrate the fabrication of NiFe-AAO inductor.

The fabrication process introduced so far has been proved it really works on the aspect of inductance enhancement. For further performance improvement including Q factor and resonance frequency, taking several steps to remove TiN/Ti seed-layer and Si substrate underneath the coil is necessary. Coating a 23-um thick AZ 4620 to cover the whole device area and define the trench region at the center of inductor coil as shown in Fig. 2-3-1(h). Utilizing HDP-RIE to etch away the PECVD oxide, NiFe-AAO nanocomposite and TiN/Ti seed-layer, a trench can directly opened to silicon substrate as shown in Fig. 2-3-1(i), so that in the following step, XeF_2 gas can easily pass through and react with silicon. In Fig. 2-3-1(j), another dry etching treatment using XeF_2 is employed to remove the silicon substrate under the inductor coil isotropically. The etching rate of horizontal and vertical is about 1.6 μm/min, the process takes about 90 min. As can be seen, a cavity full of air is formed under the inductor. With the formation of cavity, it becomes possible that TiN/Ti can be totally etched away in a solution of acetic acid at 60°C as shown in Fig. 2-3-1(k). In the final step, a MEMS inductor integrated with NiFe-AAO ferromagnetic nanocomposite is obtained as shown in Fig. 2-3-1(l).

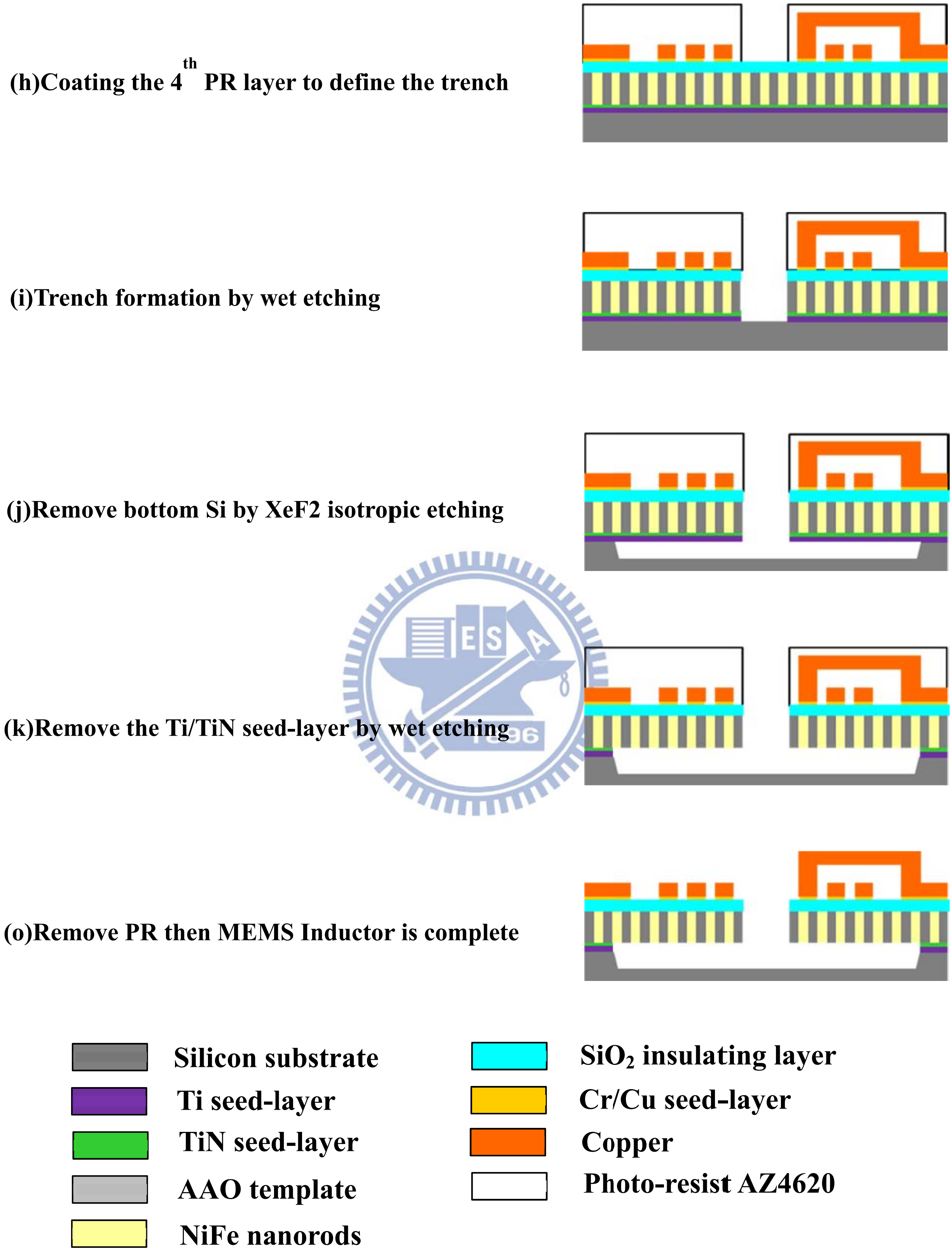

Fig. 2-3-1. The process flow of micromachined inductor incorporated with NiFe-AAO nanocomposite, step (h) to (o) demonstrate the fabrication of the micromachining process utilizing to from a suspended MEMS structure under the NiFe-AAO inductor.

The SEM photograph in Fig. 2-3-2 shows the top view of the as-fabricated NiFe-AAO inductor which is mentioned in Fig. 2-3-1(g). The SEM picture in Fig. 2-3-3 shows the top view of the micromachined inductor with NiFe-AAO nanocomposite , the depth of the silicon cavity is about 140μm. The following discussion, we'll note this kind of inductor as MEMS NiFe-AAO inductor for convenient.

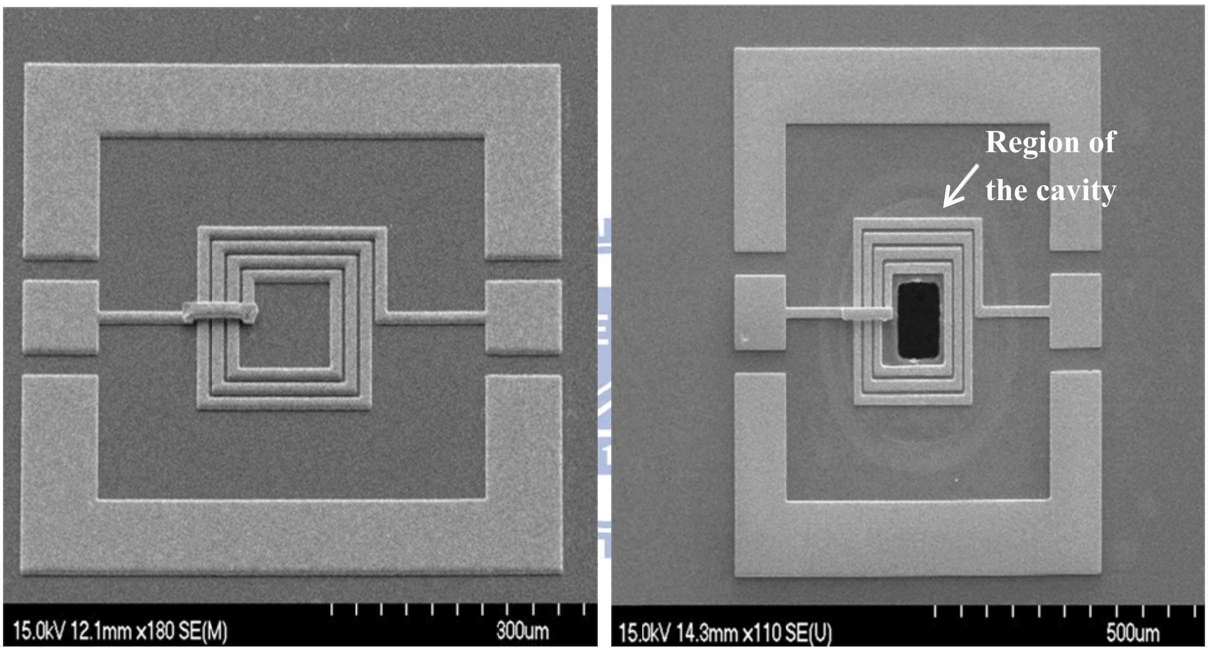

Fig. 2-3-2. The SEM photograph of (b)as-fabricated MEMS NiFe-AAO inductor. The silicon cavity underneath the nanocomposite is about 140 μm in depth.

Chapter 3 Result and Discussion

3.1 The Characterization of NiFe-AAO Nanocomposite

Magnetic property of NiFe-AAO nanocomposite measured by Vibrating Sample Magnetometer(VSM) is illustrated in Fig. 3-1-1 with two different direction of applied magnetic field, in-plane and out-plane. The relative permeability is exhibited on the hysteresis loop and can be calculated by the following formula:

$$\mu_r = 1 + {4\pi M}/{H_o} \qquad \textbf{(10)}$$

Where M is magnetization and H_0 is the applied magnetic field. The relative permeability in our case are 1.66 in out-plane applied field and 20.3 in in-plane applied field (at 100 Oe). According to Sang-Geun Cho et al[15], the critical length L_C is defined by the following equation:

$$L_C = \frac{2\pi d^3}{6.3 r^2} \qquad \textbf{(11)}$$

Where d is the inter-pore distance and r is the pore diameter, and both of them are read from Fig. 2-2-5. Taking these number into equation (11), the critical length L_C is about 236.1nm which is shorter than the real length of the nanorod(1000nm). This fact tells that the effective anisotropy field of the composite is negative and it also means that the easy axis of NiFe-AAO nanocomposite is in the direction of in-plane[15]. This result can explain the hysteresis loop in Fig. 3-1-1.

EDS analysis is also taken to see the composition of the nanocomposite, and the diagram is shown in Fig. 3-1-2. The weight composition tells us that the nanocomposite contains Nickel of 18.9% and Iron of 81.1%. This implies the ferromagnetic we have been utilized in this work is $Ni_{80}Fe_{20}$ permalloy.

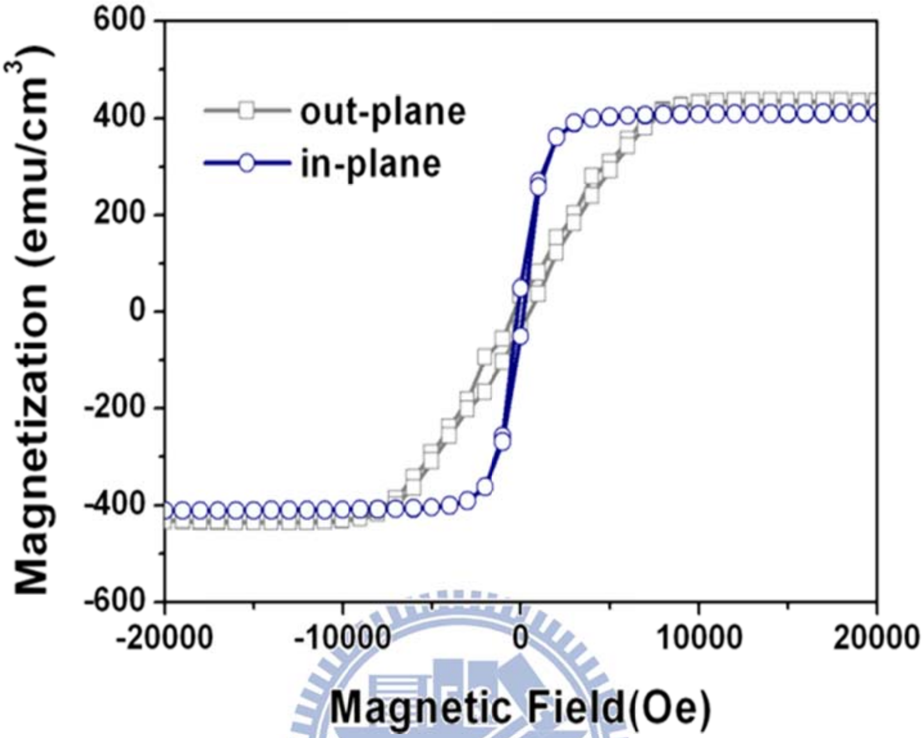

Fig. 3-1-1: The M-H loops of NiFE-AAO nanocomposite which is measured by VSM with different applied magnetic field: in-plane and out-plane.

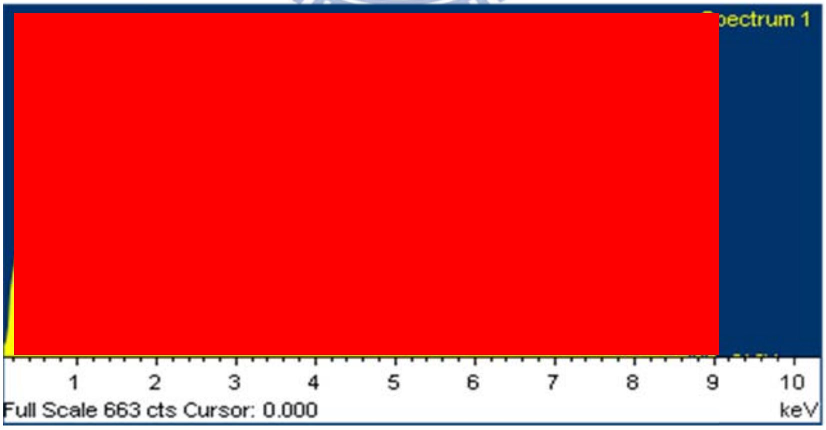

Element	Weight%	Atomic%
Fe K	18.90	19.67
Ni K	81.10	80.33
Totals	100.00	

Fig. 3-1-2: The EDS analysis of NiFe-AAO nanocomposite

In addition, the anisotropy field H_k can be read from the hysteresis loop which is 5800 Oe and the saturation magnetization M_s is 400 emu/cm^3 . So the FMR frequency of ferromagnetic film can be roughly calculated by equation (6):

$$f_{FMR} = \frac{\gamma}{2\pi}\sqrt{H_k(H_k + 4\pi M_S)} \cong 20.72GHz$$

In contrast with conventional NiFe magnetic film, the FMR of NiFe-AAO nanocomposite can be improved as high as 20.72 GHz due to large H_k.

3.2 The Performance Measurement of MEMS Inductor Combining NiFe-AAO Nanocomposite

In the work, the two ports scattering parameters (S-parameters) of the inductors are measured up to 20GHz with on RF probe station using the high frequency probes (Cascade Microtech, Inc., INIFINITY-40-GSG-100μm) and Agilent E8364B PNA network analyzer. After short-open-load-through (SOLT) calibration then measured the S-parameters. Due to on wafer open doesn't have good characteristic and accurate model for probe on the open, so the de-embedding on each device is important. The de-embedded S parameters are then transformed into Y-parameter using Agilent ADS software. The equivalent series inductance (L) and quality factor (Q) of the inductors are extracted from the Y-parameters base on the following equation [16], respectively:

$$L = Im(1/Y_{11})/2\pi f \qquad (12)$$

$$Q = Im(1/Y_{11})/Re(1/Y_{11}) \qquad (13)$$

where *f* is the signal frequency. The frequency dependence inductance and Q-factor of the as-fabricated 3.5 turns spiral inductors with NiFe nanorods core as shown in Fig.3-2-1 and Fig.3-2-2, and the corresponding air-core inductor is also shown. Fig. 3-2-1 and Fig. 3-2-2 only show the measurement report up to 5GHz due to the performance of NiFe-AAO inductor is restricted by parasitic effect within this short operating bandwidth, and the parasitic effect is going to be discussed later on. The result shows the inductance value is successfully improved up to 1 GHz with about 15% enhancement; nevertheless, this approach also accompanies two drawbacks including *Q* factor peak value decreased from 13 to 6(~55% reduction) and the self-resonance frequency also decreased from about 14GHz to 3GHz.

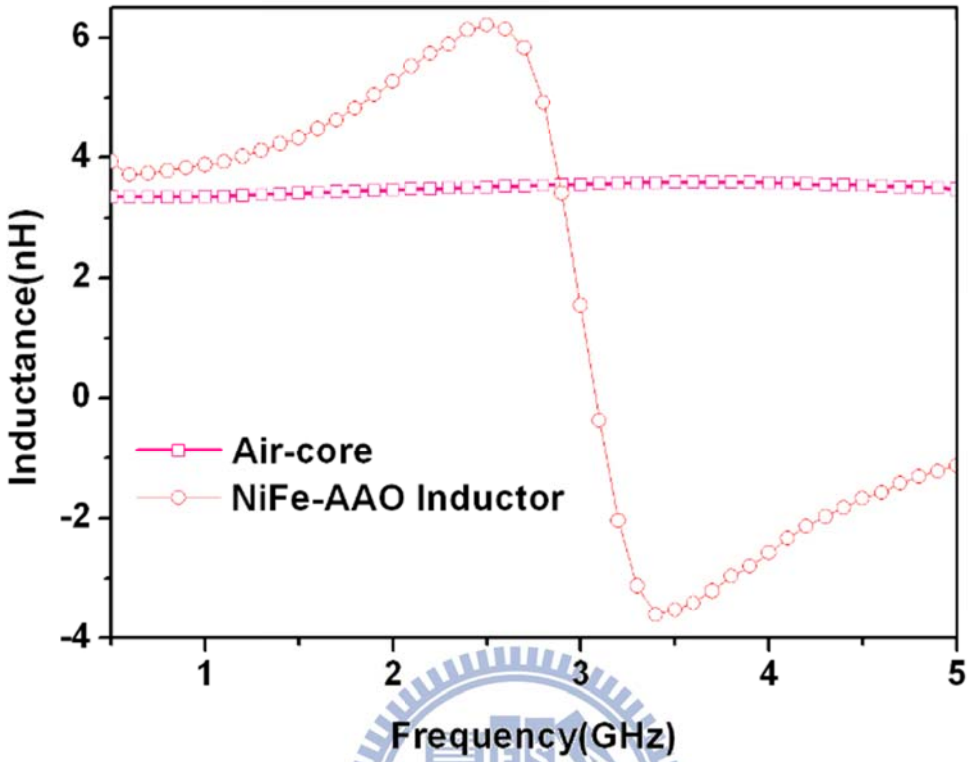

Fig. 3-2-1: The equivalent series inductance of NiFe-AAO and Air-core inductor

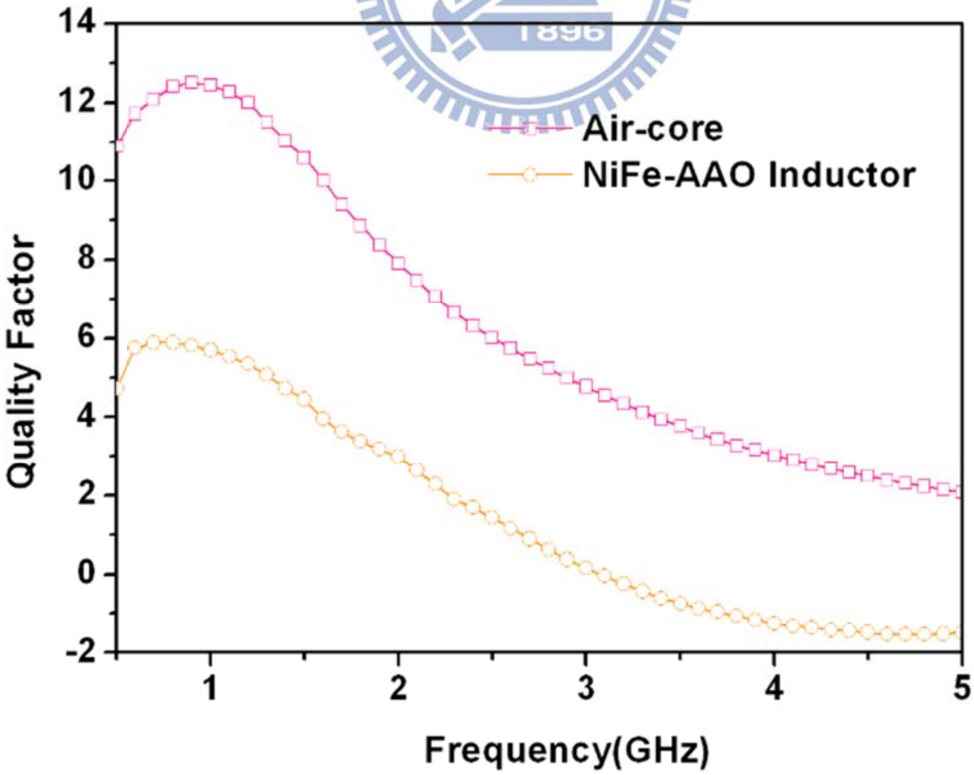

Fig. 3-2-2: The equivalent Quality factor of NiFe-AAO and Air-core inductor.

This fact is attributed to large parasitic capacitance induced by TiN/Ti seed-layer. This conductive seed-layer can be considered as the bottom electrode and thus, forms a large capacitor between insulating SiO_2 and NiFe-AAO nanocomposite. As the result, the high frequency electric field wave generated by inductor itself is prohibiting from penetrating the conductive seed-layer and soon decays to zero. The loss mechanism of this large parasitic capacitor is illustrated in Fig. 3-2-3.

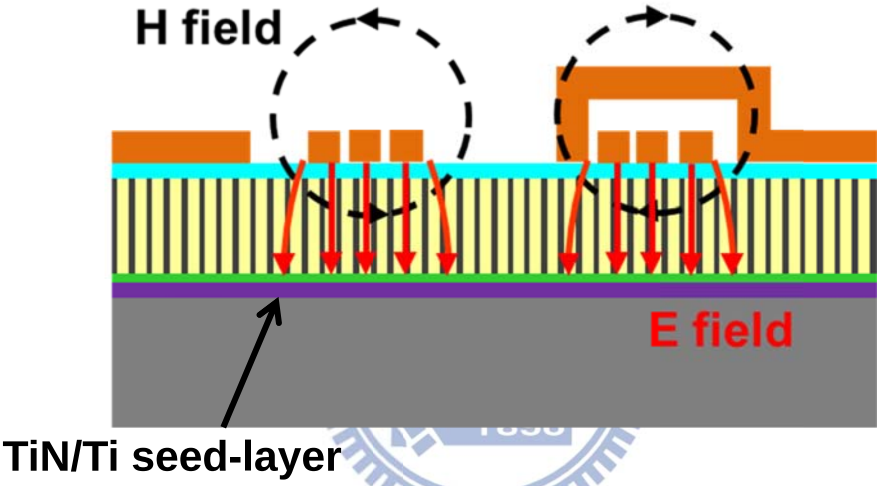

Fig. 3-2-3: The electromagnetic wave generated by the spiral inductor

Besides, the simulation software HFSS is also introduced to support this assumption. Although the number of total nanorods can’t achieve as much as the real case, owing to the limitation of the mesh elements. The purpose of this simulation is to see what happens near the conductive seed-layer, the simulated electric field contribution is illustrated in Fig. 3-2-4. From Fig. 3-2-4, the magnitude of electric field is strong in insulating layer (red region), but it decays rapidly to zero as soon as it reaches the titanium surface which is exactly matched our assumption.

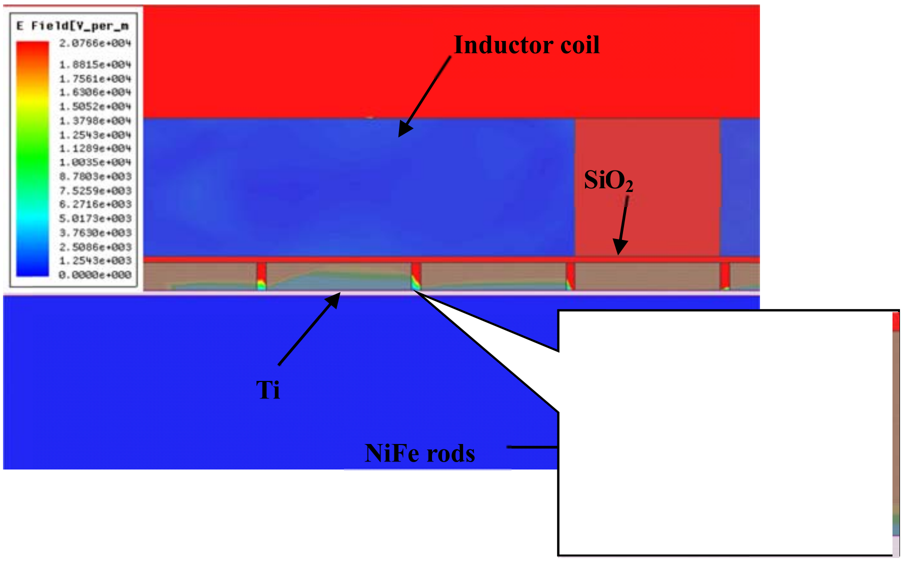

Fig. 3-2-4: The magnitude of electric field pattern simulated by ANSOFT HFSS, results indicate that the electric field decays rapidly near the Ti surface which causes more drastic parasitic effect than typical case.

In order to further discus the characteristic of spiral inductor when operating at high frequency. A conventional π-model is introduced here to help accounting for which part of the inductor causes the major power loss[17]. Each lump element from Fig. 3-2-5 are going to be used to explain the inductor's high frequency characteristic.

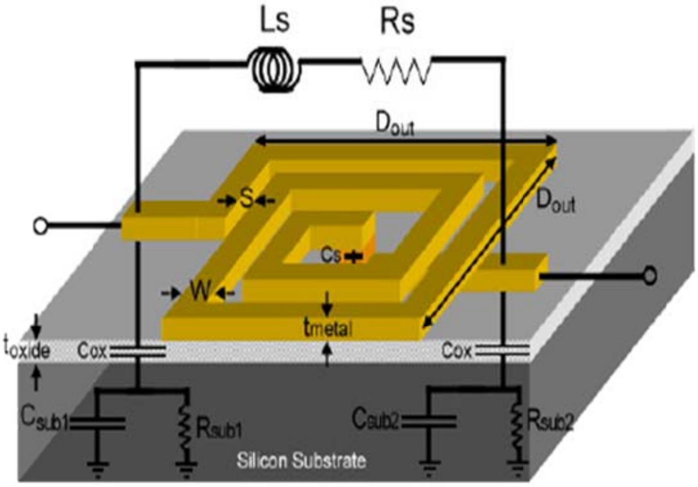

Fig. 3-2-5: The π-model of spiral inductors.

Where L_S represents the series inductance, R_S is the series inductor resistance, C_S represents the feed-through capacitance, C_{ox} stands for the oxide capacitance between spiral coil and substrate. The parasitic substrate capacitance and resistance are modeled by C_S and R_S respectively. And A Quality factor of spiral inductors can be calculated by the following[18]:

$$Q = \frac{\omega L_S}{R_S} \cdot \frac{R_P}{R_P + [(\omega L_S / R_S)^2 + 1] R_S} \cdot [1 - \frac{R_S^{\,2} (C_S + C_P)}{L_S} - \omega^2 L_S (C_S + C_P)] \qquad \textbf{(14)}$$

Where $$C_P = C_{ox} \cdot \frac{1 + \omega^2 (C_{ox} + C_{sub}) C_{sub} R_{sub}^{\,2}}{1 + \omega^2 (C_{ox} + C_{sub})^2 R_{sub}^{\,2}} \qquad \textbf{(15)}$$

Also, according to our measurement results, the value of these lumped-components can be extracted as shown in Table. 3-1.

	Air-core inductor	**NiFe-AAO inductor**
Ls	3.3nH	3.75nH
Rs	0.627Ω	0.83Ω
Cs	25.88fF	*27.4fF*
C_{ox}	1.05pF	6.36pF
C_{sub}	13.28fF	
R_{sub}	180Ω	
C_{AAO}		0.86pF
R_{AAO}		50Ω

Table. 3-1: Extracted elements of the spiral inductor model with and without NiFe core.

And a conventional nine elements π-model is applied for easily understanding the loss mechanism between these two kinds(NiFe-AAO inductor and Air-core inductor) which is shown in Fig. 3-2-6[19]. In comparison with the model stands for air-core inductor as in Fig. 3-2-6(a), the case of NiFe-AAO inductor doesn't see the silicon substrate parasitic effect due to the continuous Ti seed-layer inhibits electromagnetic wave penetrating through it and the substrate parasitic effect is replaced by the capacitance (C_{AAO}) and resistance (R_{AAO}) generated within the nanocomposite. Recall the simulation electric field pattern in Fig. 3-2-4, the magnitude of electric is strong around the inductor coil and suddenly decays when it approaches the surface of Ti, so we can't see any electric field distribution in the underlying silicon substrate.

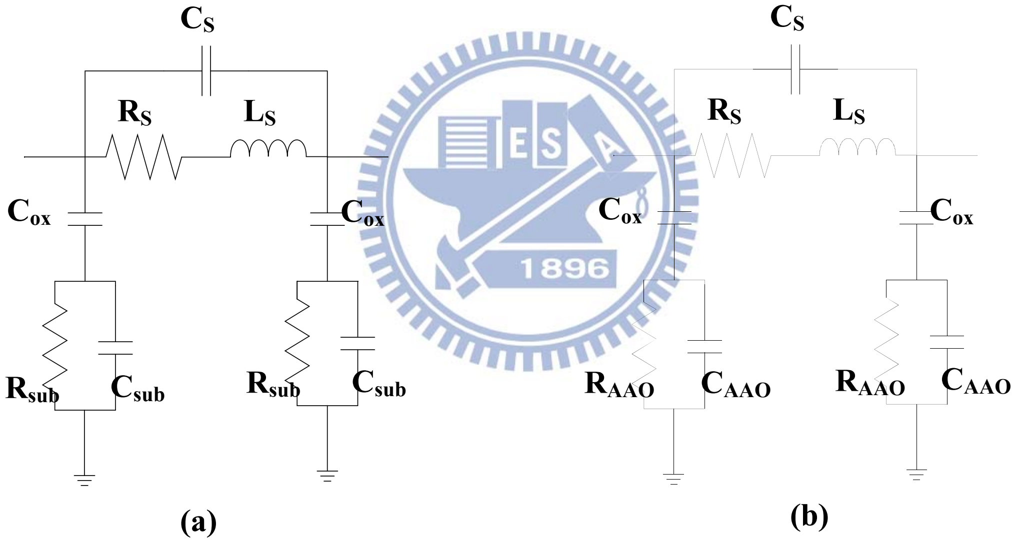

Fig. 3-2-6: The π-model of (a) Air-core inductor and (b) NiFe-AAO inductor

In lower frequency (<1GHz) range, the right term of both numerator and denominator in equation (12) are less than 1, so the parasitic capacitance(C_P) is almost dominate by oxide capacitance(C_{ox}). The larger this capacitance is, the more energy dissipation it will take, so smaller *Q* factor can be estimated in the case of NiFe-AAO inductors from the information in Table. 3-1.

When the operating frequency is much higher, e.g. near self-resonance frequency. The both right term of numerator and denominator in (15) are larger than 1,

$$C_P \cong \frac{C_{OX}C_{sub}}{C_{OX}+C_{sub}} \cong C_{sub}$$

so C_P is closely in the form like C_{ox} and C_{sub} are connecting in series. Due to C_{ox} is at least 50 times larger than C_{sub}, the value of C_P is almost equal to C_{sub}. The resonance occurs when the value *Q* factor is zero[7], so the resonance frequency can be obtained by setting equation(11) equal to zero as following:

$$\omega_{res} = \sqrt{\frac{1}{L_S(C_S+C_P)} - \frac{R_S{}^2}{L_S{}^2}} \approx \sqrt{\frac{1}{L_S(C_S+C_P)}} \qquad \textbf{(16)}$$

Recall that, C_P is almost C_{sub} when the operating frequency is near resonance frequency, so the self-resonance frequency of a inductor is not only decided by it's own intrinsic capacitance C_S but also be affected by the parasitic capacitance C_{sub}. Base on this conception, the substrate capacitance(C_{AAO}) induced by TiN/Ti seed-layer is much bigger than it is in the case of air-core inductor, as the result, the self-resonance frequency is very small. Basing on these analysis, removing the TiN/Ti seed-layer is necessary to improve the whole performance.

The existence of TiN/Ti seed-layer forbids the electromagnetic wave passing through, and cause large power dissipation and parasitic capacitance to limit the operating bandwidth in high frequency range. Removing the TiN/Ti seed-layer totally is prior mission. Fig. 3-2-7(a) shows the measurement inductance of MEMS NiFe-AAO inductor, fortunately, about 15% inductance enhancement still remains the same after removing the center part of magnetic nanocomposite which implies that the contribution of inductance enhancement is attributed to the magnetic cores under the inductor coil, and this time the inductance enhancement can be further improved up to 4GHz. In Fig. 3-2-7(b), the measurement result of *Q* factor maximum of MEMS NiFe-AAO inductor is 11.16 at 1.2GHz which is almost 2 times larger than the value of as-fabricated NiFe-AAO inductor. Also, the self-resonance is shifted from 3GHz to 10GHz, these improvements can be more obviously observed than the prior approach.

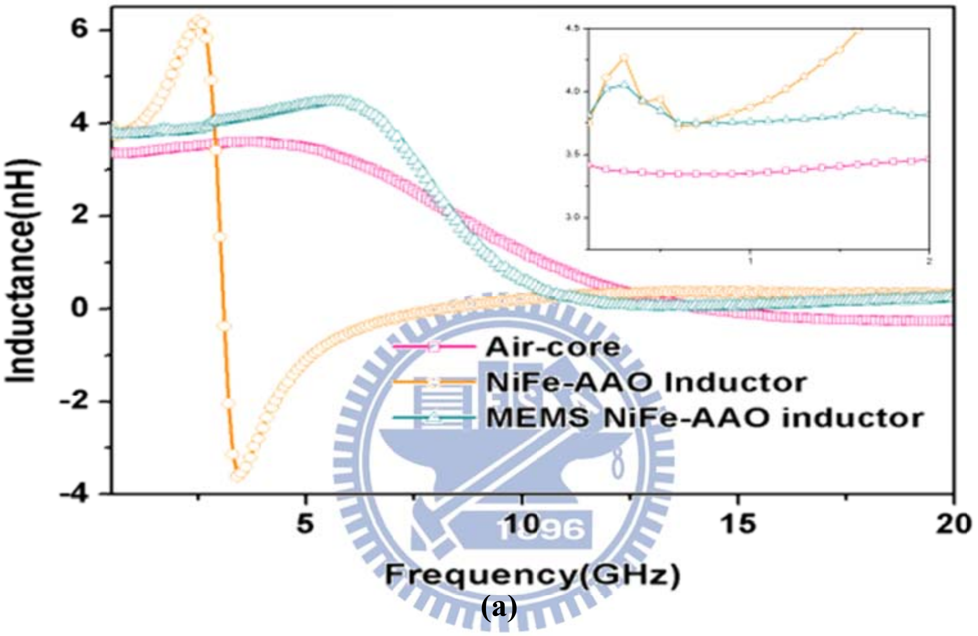

(a)

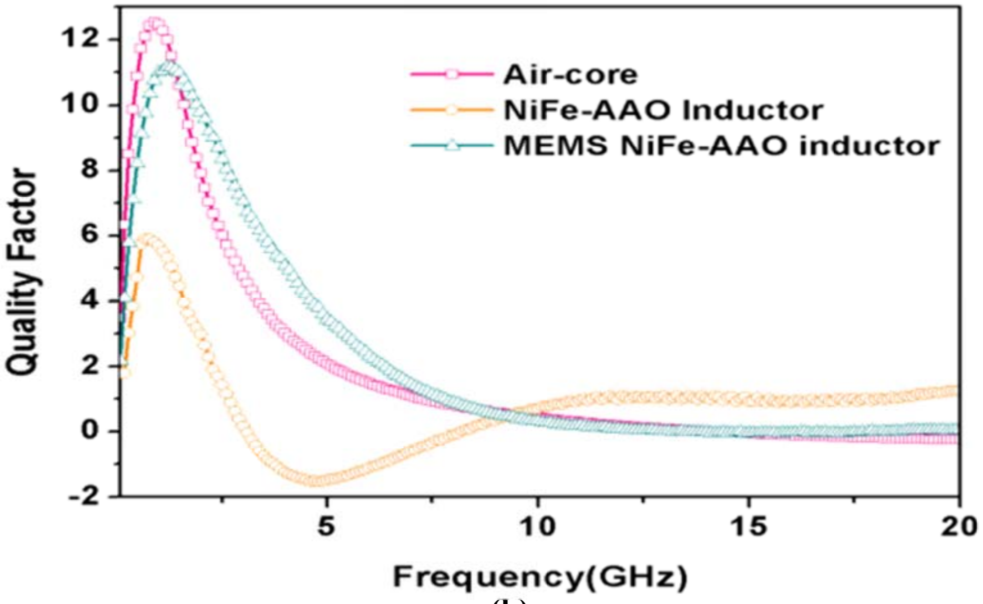

(b)

Fig. 3-2-7: The measured high frequency characteristic of MEMS NiFe-AAO inductor (a)The inductance of inductors and(b)The Quality factor of inductors

The concept of how MEMS inductors help to reduce parasitic effect is simple. By removing the substrate under the coil, the magnitude of induced ECL can be diminished and also provide a small capacitance C_{air} connecting in series with C_{ox}[2]. So a high *Q* inductor with high resonance frequency is achieved. In general, the *Q* factor of a MEMs inductor is at least 20, and the resonance frequency over 20GHz is easily accomplished. Even if we utilized the micromachining process on NiFe-AAO inductor to improve the performance, there is still a distinction on the performance behavior between this work and typical MEMS inductor. So there must be some parasitic effect owing to the existence of NiFe-AAO nanocomposite. The following is going to discuss the effect caused by the nanocomposite, and simulation software ANSOFT HFSS is used to help understanding the mechanism.

The simulation set up is from 0.1GHz to 30GHz. The morphology of the simulation model is shown in Fig. 3-2-8(a), the spiral inductor here is in the same dimension as we use in the real case, for convenience, choosing Ni as the magnetic material in this simulation and is also surrounded by alumina oxide. The square Ni rods is designed due to soft wear can easily analyze than in the shape of cylindrical. The Ni array is arranged in the porous alumina oxide just like AAO but large amount of porous number requires large mesh of simulation, so the array is designed in three cases with different number of elements of the array, they are 26x26, 36x36, 46x46 in number of elements respectively. The spacing between element to element are 5-um, 2.5-um, 0.625um respectively. The results of these three cases are compared to typical MEMS inductor, both simulation results including *Q* factor and inductance are shown in Fig. 3-2-8(c), (b). In comparison with the typical MEMS inductor, the *Q* factor and resonance frequency reduction are in proportional to the total number of array elements. This is because of that, as the number of elements is increasing, in the same time, they are getting closer to each other which cause large conducting area under the inductor and in the same time, enlarge the capacitance between rods.. The electromagnetic wave soon decays when it touches the surface of Ni array, so the both *Q* factor and resonance frequency will become much smaller. The case of MEMS inductor with 46x46 Ni array is the limitation of software and is much like our realistic case, so the following we're going to choose the one for further discussion in detail.

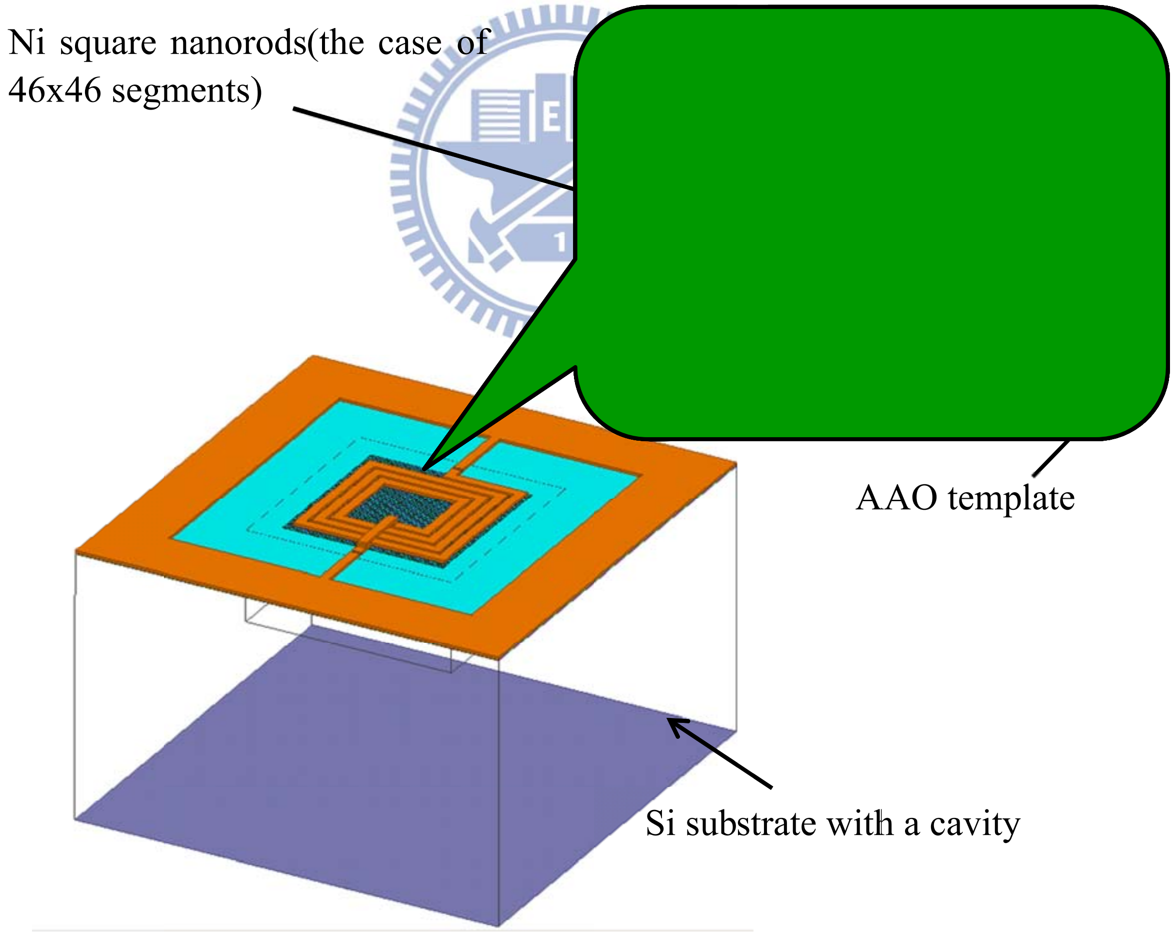

(a)

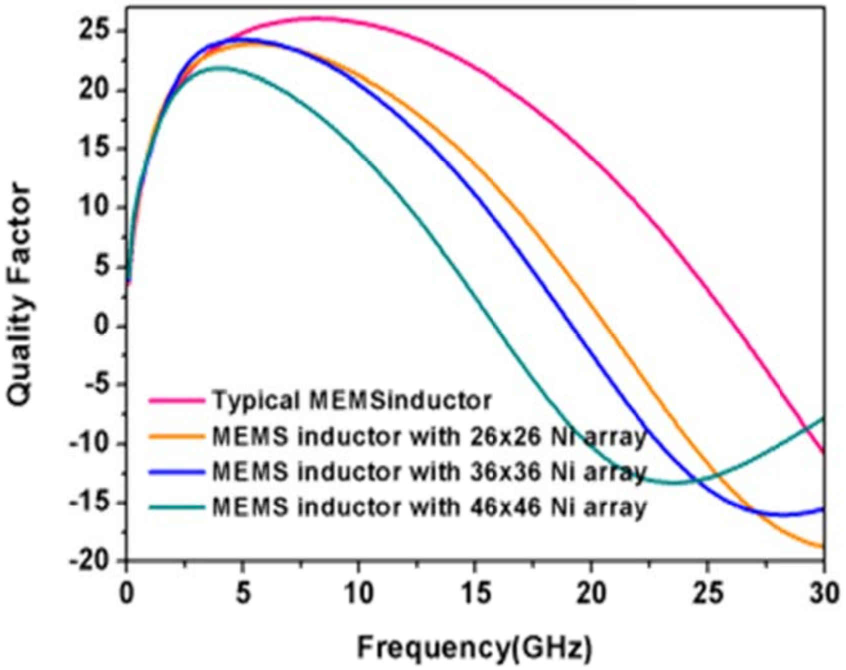

(b)

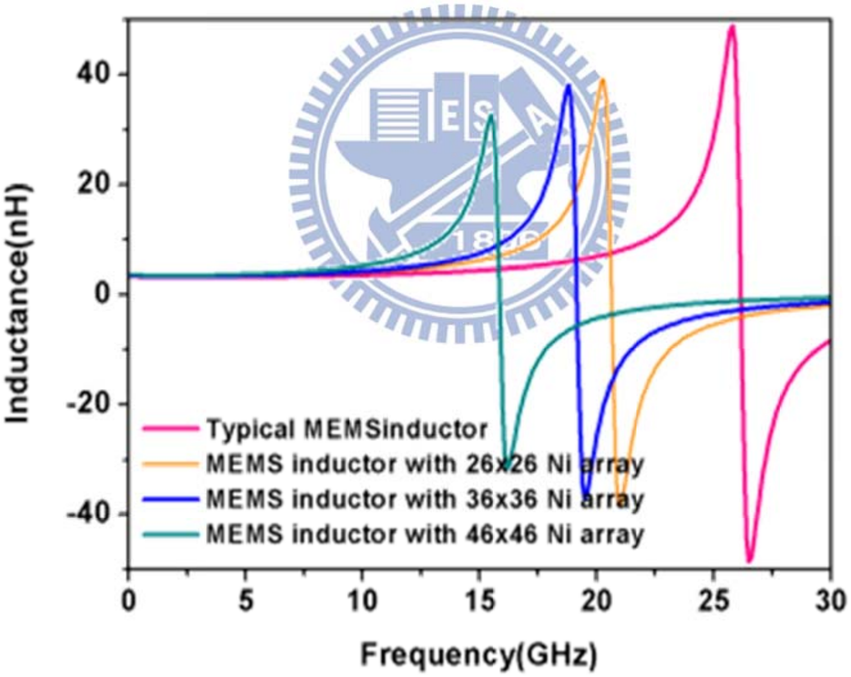

(c)

Fig. 3-2-8: The simulation model is constructed by ANSOFT HFSS and it's morphology is depicted in(a), the inductor is the same as the one of real case which is also designed with n=3.5, d_{in}=100um and the magnetic material is Ni and is in the shape of square for reducing the total number of mesh to obtain more array elements. The simulation sweep is taken from 0.1 GHz to 30 GHz, simulated results including Q factor and inductance value are shown in (b) and (c).

So far, we have a conclusion that the reduction of Q factor is in proportional to the conductivity of the NiFe-AAO template, but we still haven't figure out that which parasitic capacitance has the major influence on the reduction of resonance frequency. The following simulation is going to aim at the problem so that we can find the way out. The case of MEMS inductor with 46x46 Ni array will take into consideration, and the underlying insulating silicon dioxide and alumina oxide will be removed respectively to see which affects resonance frequency the most. The results are shown in Fig. 3-2-9.

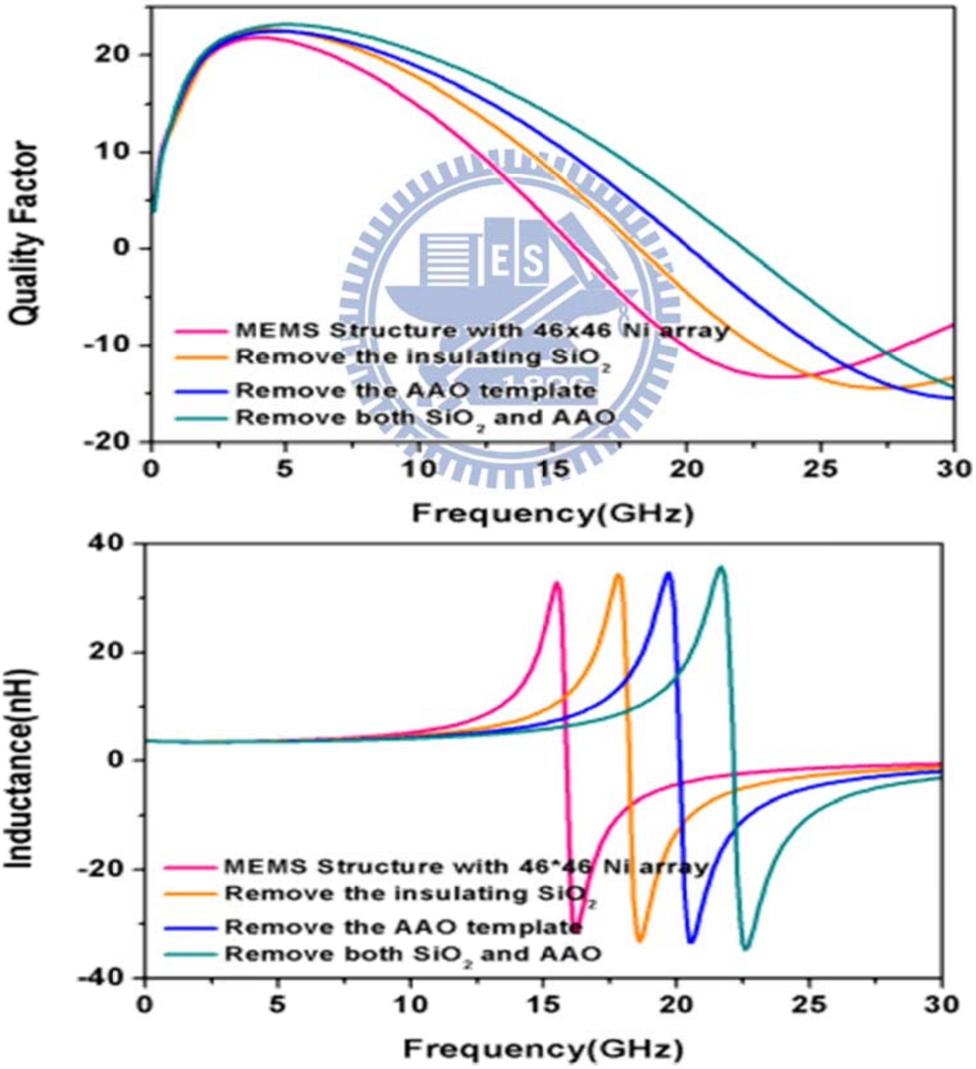

Fig. 3-2-9: The case of MEMS inductor with 46x46 Ni array is taken to compare the results of removing silicon oxide, removing AAO template and removing both of them respectively.

From the results showed in Fig. 3-2-9, by removing the insulating silicon dioxide, the resonance frequency is improved from 16.1 GHz to 18 GHz, the oxide capacitance seems not to be the major parameter to effect the resonance. By removing the alumina oxide template, the resonance frequency is obviously improved from 16.1 GHz to 21 GHz, that is, the parasitic capacitance between nanorods(C_{AAO}') is the major contribution to the reduction of resonance frequency. Therefore, in the realistic case, there is also a capacitance connected the neighboring NiFe nanorods.

The equivalent circuit that represents the whole system is too complicate to demonstrate here, so we just take one short piece for an example to investigate how it influents resonance frequency, the diagram is shown in Fig. 3-2-10(a)(b). According to Miller Theorem, the capacitance within AAO template(C_{AAO}'), connecting two nodes with two nodal voltages V_1 and V_2, can be replaced by two branches connecting the corresponding nodes to ground with the capacitance respectively $(1\text{-}K)C_{AAO}$ and $(1\text{-}K^{-1})C_{AAO}$, where $K=V_2/V_1$[20]. In order to compute the voltage ratio K, we also need to label to node voltage V_x and V_y. Assume the current flow in one port is I at that instant and flow out from the other port with the magnitude of I-dI. Applying Kirchhoff's current law, every current flows through these four nodes are listing as following:

Vx node:

$$I = \frac{V_x - V_y}{\frac{1}{SC_s}} + \frac{V_x - V_y}{R_s + SL_s} + \frac{V_x - V_1}{\frac{1}{SC_{ox}}} \tag{17}$$

Vy node: $$\frac{V_x - V_y}{\frac{1}{SC_s}} + \frac{V_x - V_y}{R_s + SL_s} = (I - dI) + \frac{V_y - V_2}{\frac{1}{SC_{ox}}} \quad (18)$$

V1 node: $$\frac{V_x - V_1}{\frac{1}{SC_{ox}}} = \frac{V_1 - V_2}{\frac{1}{SC_{AAO}'}} + \frac{V_1}{\frac{\frac{1}{SC_{air}} \bullet (\frac{1}{SC_{sub}} // R_{sub})}{\frac{1}{SC_{air}} + (\frac{1}{SC_{sub}} // R_{sub})}} \quad (19)$$

V2 node: $$\frac{V_y - V_2}{\frac{1}{SC_{ox}}} + \frac{V_1 - V_2}{\frac{1}{SC_{AAO}'}} = \frac{V_2}{\frac{\frac{1}{SC_{air}} \bullet (\frac{1}{SC_{sub}} // R_{sub})}{\frac{1}{SC_{air}} + (\frac{1}{SC_{sub}} // R_{sub})}} \quad (20)$$

The purpose of equation (17), (18), (19) and (20) is to get the ratio between V_1 and V_2, so we don't need to focus on solving these four node voltage. The Miller coefficient K can be calculated and its value is -1 by assuming dI is very small. So C_{AAO}' is replaced by two equal branches of capacitors, each of them is two times larger than C_{AAO}' and is shown in Fig. 3-2-10(c). These two branches of Miller capacitor are connected in parallel with the original shunt branch, the total parasitic capacitance(C_P) is still enlarged, even though C_{air} is quiet small. And that's the reason why combining the NiFe-AAO nanocomposite for inductance enhancement but still can't catch up typical MEMS inductor on the aspect of Q factor and resonance frequency.

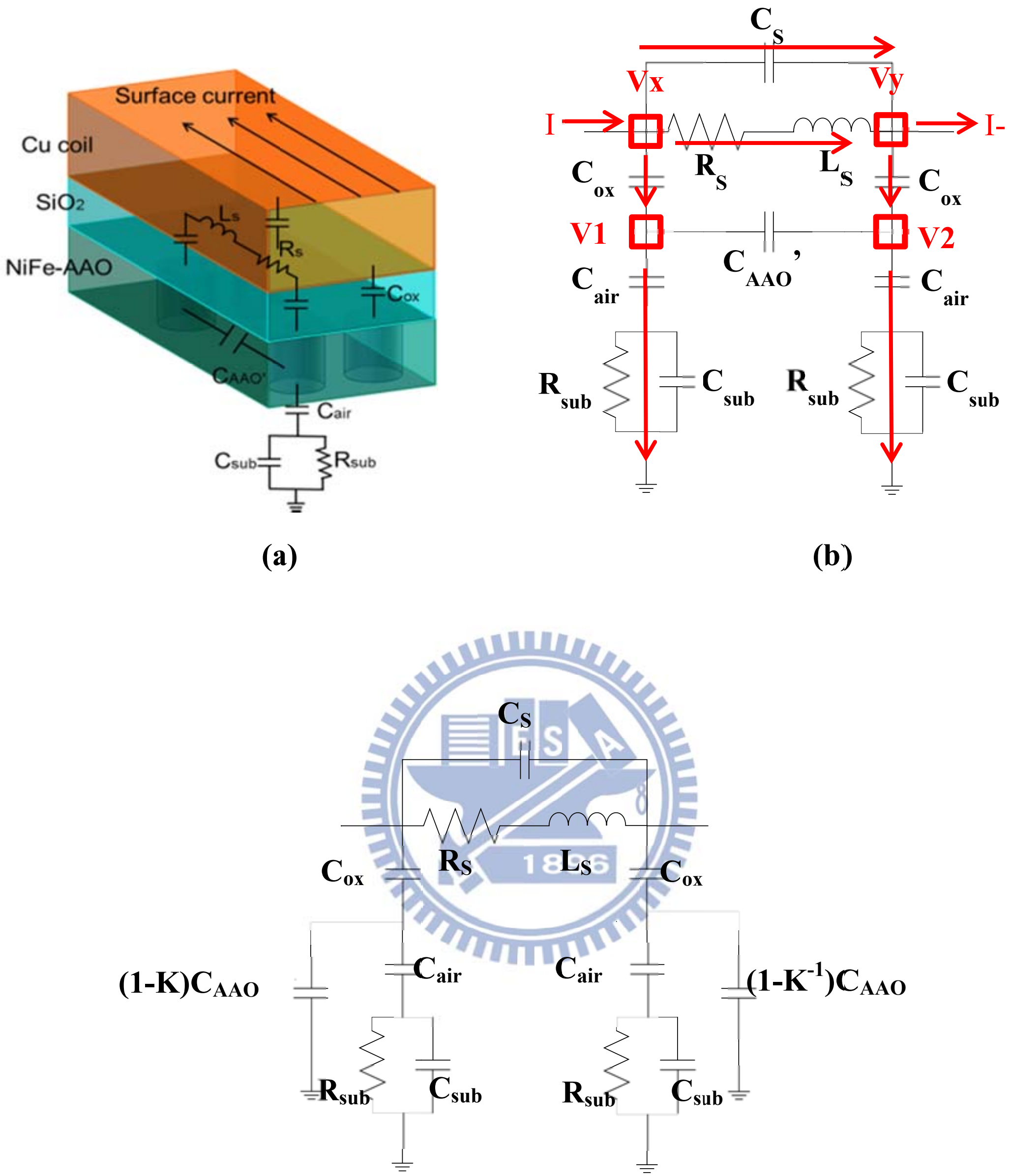

(a) (b)

(c)

Fig. 3-2-10: The diagram in (a) shows the π-model of the MEMS NiFe-AAO inductor in a short piece, and the Miller coefficient can be calculated by two nodal voltages V_1 and V_2 as labeled in (b), applying Miller Theorem, C_{AAO}' can be divided in two branches of capacitor as shown in (c)

Chapter 4 Conclusion and Future Work

4.1 Conclusion

The inductance enhancement of on-chip inductor have been successfully demonstrated up to 1GHz by integrating NiFe-AAO nanocomposite core, and can be further improved up to 4GHz after introducing a micromachining process to remove the TiN/Ti seed-layer. Both Q factor and resonance frequency can be further improved simultaneously. Although the performance is not as perfect as the typical MEMS inductor due to the parasitic capacitance generated within the nanocomposite, some research efforts are still needed by applying high resistivity ferrite to replace the permalloy core for further eliminating the parasitic effects for high performance RFIC applications

4.2 Future Work

Recalling the simulation results in Fig. 3-2-9, the performance can be further improved by removing both insulating oxide layer and AAO template. If we want to achieve much excellent performance, the electrical insulating layer may be chosen like low-K dielectric material to reduce the capacitance within this dielectric layer. Moreover, the parasitic capacitance between nanorods can be eliminated by choosing some less conductive ferrite material for substitution, for example iron oxide may be a considerable choice[21].

Reference

[1] D. Shaeffer and T. Lee, "A 1.5-V, 1.5-GHz CMOS low noise amplifier," *IEEE Journal of Solid-State Circuits*, vol. 32, no. 5, pp.745-759, May. 1997.

[2] Sheng-Hsiang Tseng and Ying-Jui Hung,"A 5.8 GHz VCO with CMOS-compatible MEMS inductors," *Sensor and Actuators A: Physical*., vol. 139, no. 1-2, pp. 187-193, 2006.

[3] S. Bantas and Y. Koutsoyannopoulos, "CMOS Active-LC Bandpass Filters With Coupled-Inductor Q-Enhancement and Center Frequency Tuning," *IEEE Trans. on circuits and systems*, vol. 51, no. 2, pp. 69-76, Feb. 2004.

[4] J. Kim, W. Ni, C. Lee, E. C. Kan, I. D. Hosein, Y. Song, and C. Liddell, "Magnetic property characterization of magnetite (Fe3O4) nanorod cores for integrated solenoid rf inductors," *J. Appl. Phys*., Vol. 99, No. 8, pp.08R903-08R903-3, Apr. 2006.

[5] T.Y. Chao, H.F. Hsu, K.M. Chen and Y.T. Cheng, "NiFe-AAO Nanocomposite for Performance Enhancement of On-chip spiral inductors" in *Proc. Transducers 2011*, Beijing, China, Jun. 5-9, 2011.

[6] M.C. Hsu, T.Y. Chao, Y.T. Cheng, C.M. Liu, and C.C. Chen, "The Inductance Enhancement Study of Spiral Inductor Using Ni-AAO Nanocomposite Core," *IEEE Trans.Nano*., vol. 8. no.3, May 2009.

[7] C.Y. Yue and S.S. Wong, "On-chip Spiral Inductors with Patterned Ground Shields for Si-based RFIC's," in Proc. *IEEE, JSSC*, vol. 33,no.5,pp. 743-753, May.1998.

[8] S. Shingubara, "Fabrication of Nanomaterials Using Porous Alumina Templates," *J. Nanopart. Res.,* Vol. 5, pp. 17-30, Apr. 2003.

[9] M. M. Sinha, and J. S. Kim, “Analysis of Vibrational Modes and Phonon Density of States of Aluminate Spinels,” *J. Korean Phys. Soc.*, Vol. 43, No. 2, pp. 237-241, Aug. 2003.

[10]C. M. Liu, and C. Chen, “Microstructure and Magnetic Properties of Nickel Nanorod Arrays on Silicon Substrate,” *TMS Conf., TMS*, 2007

[11]Sunil Kumai Thamida and Hsueh-Chia Chang, “Nanoscale pore formation dynamics during aluminum anodization.” *AIP Chaos*, Vol. 12,No. 1,pp. 240-251,2002.

[12]M. Tian, S. Xu, J. Wang, N. Kumar, E. Wertz, Q. Li, P.M. Campbell, M.H.W. Chan and T.E. Mallouk, “Penetrating the oxide barrier in situ and separating freestanding porous anodic alumina films in one step, ” Nano Letters, vol.5, no.4, pp. 697-703, 2005.

[13]Xiaowei Zhao, Seok-Kyoo Seo, Ung-Ju Lee and Kun-Hong Lee, “Controlled Electrochemical Dissolution of Anodic Aluminum Oxide for Preparation of Open-Through Pore Structures.” J. Electrochem. Soc, vol. 154, no. 10,pp.553-557. pp. 281-285. July 2007.

[14]Rabin,O.;Herz,P.R.;Lin,Y.M.;Akinwande,A.I;Croniun,S.B. and Dresselhaus,M.S. ”Formation of thick porous anodic alumina films and nanowire arrays on silicon wafers and glass , ”*Adv.Funct.Mater*.2003,13,631.

[15]Sang-Geun Cho, Bongyoung Yoo, Ki Hyeon Kim, and Jongryoul Kim, “Magnetic and Microwave Properites of NiFe Nanowires Embedded in Anodized Aluminum Oxide(AAO) Templates.” *IEEE TRANSACTIONS ON MAGNETICS,* Vol. 46, No. 2, Feb, 2010.

[16]I. J. Bahl, “High-performance inductors,” *IEEE Trans. Microwave Theory Tech.*, Vol. 49, No. 4, pp. 654-664, Apr. 2001.

[17]De Los Santos and H.J., “On the ultimate limits of IC inductors-an RF MEMS perspective.” *Electronic Components and Technology Conference*, pp. 1027-1031, 2002.

[18]C.Y. Yue and S.S. Wong, “On-chip Spiral Inductors with Patterned Ground Shields for Si-based RFIC’s,” *in Proc. IEEE, JSSC*, vol. 33,no.5,pp. 743-753, May.1998.

[19]C. Patrick Yue and S. Simon Wong, ”Phisical Modeling of Spiral Inductors on Silicon,” *IEEE TRANSACTIONS ON ELECTRON DEVICES, vol. 47,no. 3,pp.560-568, Mar. 2000.*

[20]John M. Miller, "Dependence of the input impedance of a three-electrode vacuum tube upon the load in the plate circuit," *Scientific Papers of the Bureau of Standards*, vol.15, no. 351, pages 367-385, 1920.

[21]V. Markovac and M. Cohen, “The Anodic Deposition of Iron Oxide Films on Iron,” *J.Electrochem.Soc.*, vol. 114, no. 7, pp.674-678, 1967.

Vita

姓　　名：陳冠名 (Kuan-Ming Chen)

出生日期：中華民國七十三年十二月五日

出 生 地：台北縣

E - mail：edmund.ee97g@nctu.edu.tw

學　　歷：

私立協同高級中學 (2000.9～2003.6)
(Concordia Middle High School)

國立彰化師範大學機電工程系 (2003.9～2008.6)
(Department of Mechatronics Engineering, National Changhua University of Education)

國立交通大學電子工程所碩士班 (2008.9～2011.10)
(Department of Electronics Engineering & Institute of Electronics, National Chiao Tung University)